



University dissertation to obtain the academic degree
Master of Science in Mechanical Engineering
(Laurea Magistrale in Ingegneria Meccanica)
From Politecnico di Torino

Numerical optimization of an enhanced linear Fresnel collector equipped with Raschig Rings porous medium

Supervisor:

Prof. Laura Savoldi

Eng. Hossein Ebadi

Candidate:

Ahmed Salaheldien Seidahmed Alamin

Academic year 2021

ACKNOWLEDGEMENTS

Firstly, I would like to take this opportunity to express my thanks and gratitude to my supportive supervisor Professor Laura Savoldi who has supported me throughout this thesis. Her help and guidance through the weekly meetings to discuss the tasks of the research project was a steppingstone to perform my research thesis. In addition, a special mention is given to the PhD student Mr. Hossein Ebadi. The discussions with him helped me to overcome the many challenges and difficulties endured during the thesis and to proceed with my research. I would like also to thank HPC at Politecnico di Torino.

Above all, to almighty Allah for the guidance to conduct my research thesis in the prestigious university Politecnico di Torino in Italy.

Last but not least, my parents and brother who always have shown their support. Without them, I would not be able to reach this point. My love and gratefulness to them are beyond any words.

ABSTRACT

Solar collector absorber tubes have an important role in converting solar radiation into absorbing thermal energy and transferring it to heat transfer fluid. In this work the linear Fresnel receiver tube has been evaluated using 3D Computational Fluid Dynamics (CFD), by using commercial software STAR CCM+.

In this study a single horizontally absorber tube with air was investigated in turbulent flow using k - ϵ Realizable model. CFD analysis was used to obtain thermodynamic data for the development procedure. The comparison between single tube and porous medium with constant heat flux is done through CFD to analysis the effect of porous medium thermally and dynamically.

Finally, it has been obviously shown that Raschig rings increase the heat transfer between fluid and solid part. In contrast, the pressure drop of tube with Raschig rings has higher value due to porosity and volume of porous medium.

Keywords: CSP, Linear Fresnel collector, Air, CFD, Raschig rings.

Table of contents

ACKNOWLEDGEMENTS	II
ABSTRACT	III
NOMENCLATURE.....	0
CHAPTER ONE	2
INTRODUCTION.....	2
1.1 Background and linear Fresnel	2
1.2 Receiver	4
1.3 Techniques to improve the thermal performance	5
1.3.1 Nanofluids.....	5
1.3.2 internal fins	6
1.3.3 Porous medium	7
1.4 Purpose of Study	8
CHAPTER TWO	9
CFD ANALYSIS AND SIMULATIONS SETUP	9
2.1 Geometry.....	9
2.2 Computational fluid dynamics.....	10
2.3 Grid independence study	11
2.4 Simulation setup	13
2.4.1 Hydraulics	14
2.4.1.1 Full pipe Air.....	14
2.4.1.2 Full pipe water	16
2.4.1.3 Half pipe Air	17
2.4.1.4 Half pipe water	19
2.4.2 Thermal study	21
2.4.2.1 Full pipe Air.....	22
2.4.2.1 Full pipe water	23

2.4.2.3 Half pipe Air	25
2.4.2.4 Half pipe water	26
2.5 Preliminary Validation.....	28
CHAPTER THREE	32
RASCHIG RINGS POROUS MEDIUM.....	32
3.1 Overview of Raschig rings	32
3.2 Simulation part.....	33
Chapter four	36
Results	36
4.1 Hydraulic characteristics.....	36
4.1.1 Smooth tube	37
4.1.2 Raschig rings	40
4.2 Thermal effects	45
4.2.1 Smooth tube	46
4.2.2 Raschig rings	50
REFRENCES.....	56

List of figures

Figure 1.1 Solarmundo Fresnel prototype in Liège/Belgium	3
Figure 1.2 (a) Sketch of an LFC- receiver with an absorber tube with air stable coating, secondary receiver, and glass plate in the bottom; (b) Sketch of LFC-receiver with an absorber tube surrounded by glass envelope; the glass envelope may be evacuated.	4
Figure 1.3 Geometric depiction of the performance enhancement criteria	5
Figure 1.4 (a) thermal efficiency and (b) Heat transfer coefficient enhancement for different concentrations and cases with inlet temperature equal to 600 K	6
Figure 1.5 Temperature contours at outlet of the porous disc receiver for $H = 0.5 d_{i,w} = d_i$ and $\theta = 30^\circ$	7
Figure 1.6 (a) The relationship of Nu and λ_0 for different kinds filling (b) The relationship of the maximum circumferential wall temperature difference of the tube and Y for different filling types	8
Figure 2.1 Geometry of smooth tube	10
Figure 2.2 Pressure drop using Richardson for full pipe Air	15
Figure 2.3 Three different grids (a) coarse (b) medium (c) fine for full pipe	16
Figure 2.4 Pressure drop using Richardson for full pipe water	17
Figure 2.5 Pressure drop using Richardson for half pipe Air	18
Figure 2.6 Three different grids (a) coarse (b) medium (c) fine for half pipe	19
Figure 2.7 Pressure drops using Richardson for half pipe water	20
Figure 2.8 Outlet temperature using Richardson for full pipe Air	20
Figure 2.9 Outlet temperature using Richardson for full pipe water	20
Figure 2.10 Outlet temperature using Richardson for half pipe Air	20
Figure 2.11 Outlet temperature using Richardson for half pipe water	20
Figure 2.12 pressure drop convergence in (a) fully developed and (b) inlet velocity boundary conditions	30
Figure 2.13 Y^+ value for the wall under dynamic behavior	31
Figure 2.14 Y^+ value for the wall under heat flux	31
Figure 3.1 Geometry of the tube with Raschig rings	34
Figure 3.2 Mesh of tube with RRs on the bottom side	35
Figure 3.3 Mesh of tube with RRs on the bottom side	35
Figure 4.1 Velocity profile of smooth tube for different mass flow rates (a) 0.025 (b) 0.03 (c) 0.04 kg/s	38
Figure 4.2 Pressure distribution inside the smooth tube for different mass flow rates (a) 0.025 (b) 0.03 (c) 0.04 kg/s	40
Figure 4.3 Velocity profile of smooth tube for different mass flow rates (a) 0.025 (b) 0.03	42
Figure 4.4 Velocity profile of smooth tube for different mass flow rates (a) 0.025 (b) 0.03 (c) 0.04 kg/s	38

Figure 4.5 Friction factor comparison between smooth tube and enhanced pipes derived from numerical results	45
Figure 4.6 Average Nu number for full tube	47
Figure 4.7 Temperature of wall for the smooth tube for for different mass flow rates (a) 0.025 (b) 0.03 (c) 0.04 kg/s	49
Figure 4.8 Temperature of wall for the tube with RRs for different mass flow rates (a) 0.025 (b) 0.03 (c) 0.04 kg/s	51
Figure 4.9 Outlet temperatures comparison.....	52
Figure 4.10 Convective heat transfer coefficient comparisons.....	52
Figure 4.11 Average Nu comparisons	53

List of Tables

Table 2.1 simulation parameters	14
Table 2.2 The calculation results for pressure drop in different grides for full pipe Air.....	14
Table 2.3 The calculation results for pressure drop in different grides for full pipe water	16
Table 2.4 The calculation results for pressure drop in different grides for half pipe Air	17
Table 2.5 The calculation results for pressure drop in different grides for half pipe water.....	20
Table 2.6 The calculation results for temperatures in different grides for full pipe Air.....	22
Table 2.7 The calculation results for temperatures in different grides for full pipe water	24
Table 2.8 The calculation results for temperatures in different grides for half pipe Air	25
Table 2.9 The calculation results for temperatures in different grides for half pipe water.....	27
Table 2.10 validation results	29
Table 3.1 Mesh result of tube with Raschig rings	34
Table 4.1 Pressure drops, and friction factor results for smooth tube	37
Table 4.2 Pressure drops, and friction factor results for tube with RRs	41
Table 4.3 Average Nusselt correlation results	46
Table 4.4 Average Nusselt obtained from Star ccm+	47
Table 4.5 Average Nu number for smooth tube	48
Table 4.6 Average Nusselt results for tube with RRs.....	50

NOMENCLATURE

CFD	Computational Fluid Dynamics
CSP	Concentrated Solar Power
LFC	Linear Fresnel Collector
HTF	Heat Transfer Fluid
SST	Shear Stress Transport
GCI	Grid convergence index
RRs	Raschig rings
HTC	Heat Transfer Coefficient, $\text{W/m}^2/\text{K}$
A	area, m^2
D_i	internal diameter of tube, m
r_i	internal radius of tube, m
L	Length of tube, m
u	Flow speed, m/s
q	Heat flux per unit area, W/m^2
Q	useful heat, W
r	refinement ratio
h	grid size
$\Delta x, \Delta y, \Delta z$	Cartesian coordinates, m
N	total number of cells
ΔV	total volume of domain, m^3
p	order of convergence
f	friction factor
V	volume flow rate, m^3/s
Re	Reynolds number
P_r	Prandtl number
Nu	Nusselt number

h_m	Average convective heat transfer coefficient, W/m^2K
\dot{m}	mass flowrate (kg/s)
T	temperature (K)
k	thermal conductivity (W/m/K)

Greek symbols

ε	difference result between simulations value
φ	the simulation value of the variable on the grid
Δp	pressure drop (Pa)
ΔT	temperature difference (K)
μ	dynamic viscosity (Pa·s)
ρ	density (kg/ m^3)

Subscripts

th	theoretical
m	mean
w	wall
f	fluid
S	Surface
in	inlet
out	outlet

CHAPTER ONE

INTRODUCTION

1.1 Background and linear Fresnel

Renewable energy technologies produce marketable energy by converting natural phenomena into useful forms of energy most technologies use the solar energy and its direct and indirect effects on the earth (solar radiation, wind, falling water and various plants, i.e., biomass), gravitational forces (tides), and the heat of the earth's core (geothermal) as the resources from which energy is produced.[1]

Concentrated Solar Power (CSP) is one of the most attractive renewable energy technologies be used as alternative to common fossil-fuel based power plants. Solar power is indeed the most abundant available energy source to produce green and environment friendly power, exceeding world's energy demand several thousand times.[2]

Concentrated solar power (CSP) is an approach to generating electricity through mirrors. The mirrors reflect, concentrate, and focus natural sunlight onto a specific point, which is then converted into heat. The heat is then used to create steam, which drives a turbine to generate electrical power. The process can be repeated continuously because CSP technology can store the heat produced. It can therefore be used on days where there is no sun, or before sunrise and after sunset. [3]

CSP technologies are classified into four types: parabolic trough, linear Fresnel, central-receiver, and dish/engine. The first three often combine with a utility-scale power cycle such as a Rankine steam cycle to produce electricity and can be enhanced with large-scale thermal storage to increase the dispatchability of a solar power plant; the dish/engine technology uses a compact Stirling or Brayton engine to generate electricity and is more suitable for modular power generation systems (on the order of 1–30 kWe)[4]

Generally, an LFR solar collector consists of three main components: mirror field, receiver and tracking system. The direct solar radiation can be reflected by an

array of parallel mirrors to a fixed focal line at which the receiver is mounted. One of the predominant merits of LFR solar collector is that it requires minimal manufacturing, operation, and maintenance costs.[5]

The first company that constructed a prototype was Solarmundo from Belgium. Solarmundo started testing a 2,500 m² collector in Liège, Belgium, in 2001. They attracted attention with their claim to be considerably more cost effective than other existing radiation concentration systems.[6]



Figure 1.1 Solarmundo Fresnel prototype in Liège/Belgium

1.2 Receiver

The Linear Fresnel Collector (LFC) is a line focusing concentrating collector suitable for solar thermal power generation and production of process heat. Direct solar irradiation is reflected onto a stationary receiver by a primary mirror field, consisting of an array of elastically bent mirrors. For the reduction of optical losses, a secondary mirror is positioned above the absorber tube. This unit consisting of absorber tube, optional glass covers, and secondary mirror that is called the (cavity) receiver of the LFC.[7]

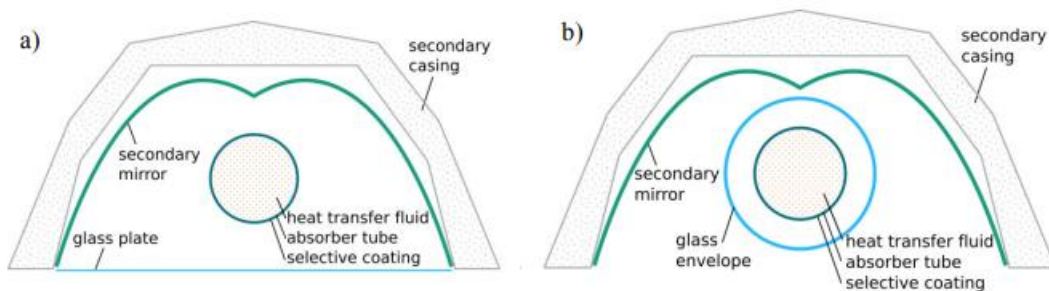


Figure 1.2 (a) Sketch of an LFC- receiver with an absorber tube with air stable coating, secondary receiver, and glass plate in the bottom; (b) Sketch of LFC-receiver with an absorber tube surrounded by glass envelope; the glass envelope may be evacuated.

The absorber tubes have a selective coating that has a high absorptance at short wave lengths and a low emittance for infrared radiation. The ISE Fraunhofer Institute in Freiburg/Germany developed a tube for Fresnel power plants with a cermet coating. Cermet is a composite material composed of ceramic and metallic materials. The coating has been proven to be stable until more than 450°C. The cermet layer, together with an antireflective layer, permits the high absorption of solar radiation, while a metallic layer reduces the emittance in the infrared range. The tubes themselves are made of stainless steel.[8]

Using thermal oil implies non-negligible installation, replacement, and disposal costs, and presents degradation at high temperatures, leakage problems leading to environmental pollution, and fire risk. Water implies the drawbacks of boiling and two-phase flow unless pressurization is achieved, increasing risks related to leakage besides freezing during cool nights and corrosion. [9]

The advantages of air, however, are counterbalanced by the lower heat transfer coefficient (HTC) with respect to liquids, which leads to higher temperatures of the tube wall and consequently higher thermal stresses, limiting the achievable solar heat flux on the absorber surface. At the same time, the heat exchange area to transfer the given thermal power needs to be increased to compensate for the low HTC, if the same temperature of liquid coolant is targeted at the outlet of the receiver.[10]

Solar thermal absorber tubes have a significant impact on the performance of solar collector systems. Thus, in this work, the focus is only on the thermal performance of the absorber tube.

1.3 Techniques to improve the thermal performance

1.3.1 Nanofluids

The flow performance criteria evaluate the heat transfer coefficient increase compared to the reference case with pure oil. This evaluation is expressed using the Nusselt number ratio (Nu/Nu_0) and the friction factor ratio (f/f_0) with three different criteria. These criteria are called Performance evaluation criteria (PEC).[11]

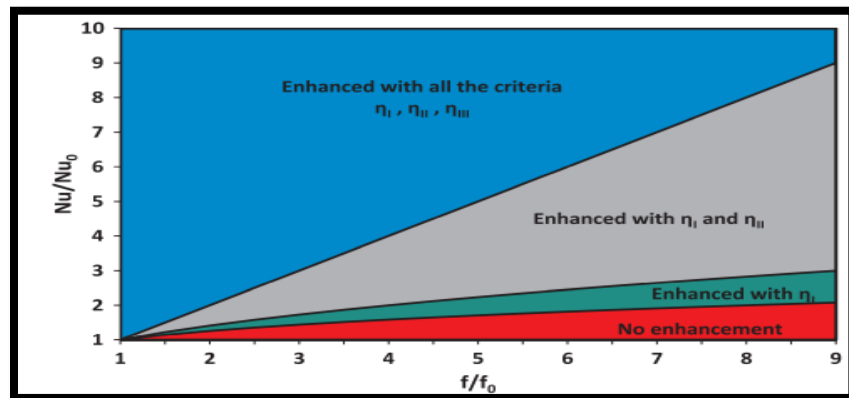


Figure 1.3 Geometric depiction of the performance enhancement criteria

The use of nanofluid can enhance the thermal performance of LFR, especially at high temperature levels. There is increased demand for pumping work which is not able to eliminate the thermal enhancement. However, a careful design of the system is needed in order the use of nanofluids to be successfully applied in Fresnel collectors.[11]

1.3.2 internal fins

It is obvious that the thermal efficiency enhancement is greater in higher inlet temperature levels because in these cases the thermal losses are greater and there is higher thermal efficiency enhancement margin. However, the results in Fig. make clearer that the internal fins lead to higher heat transfer coefficient compared to the smooth cases. The maximum heat transfer coefficient enhancement is 128% for 600 K inlet temperature, finned absorber, and nanoparticle concentration 4 and 6%.[12]

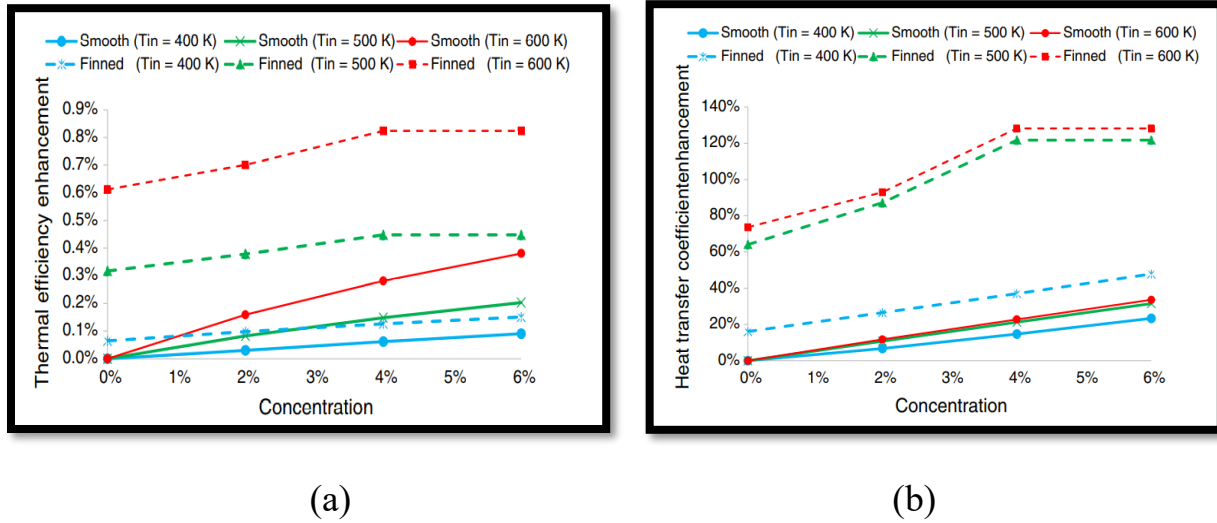


Figure 1.4 (a) thermal efficiency and (b) Heat transfer coefficient enhancement for different concentrations and cases with inlet temperature equal to 600 K

1.3.3 Porous medium

Introduction of the porous discs in the receiver, improves the heat transfer characteristics of the receiver but with a pressure drop as penalty. The heat transfer was augmented in all receivers due to increase in heat transfer area, thermal conductivity, and turbulence. The percentage increases in Nusselt number for optimum receiver configuration is 64.2% compared to tubular receiver at Reynolds number of 31,845 with the pressure drop of 457 Pa. [13]

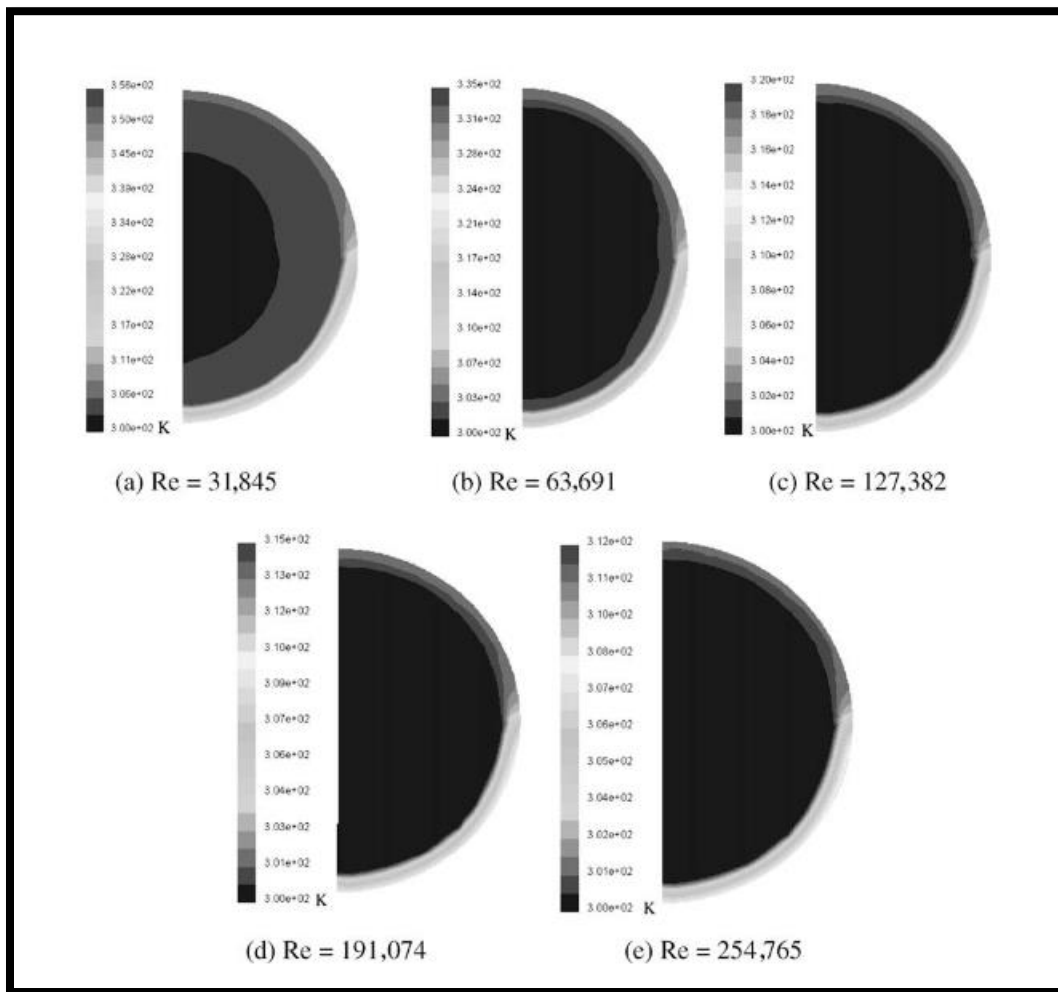


Figure 1.5 Temperature contours at outlet of the porous disc receiver for $H = 0.5 d_i$, $w = d_i$ and $\theta = 30^\circ$

In Linear Fresnel receiver tube using molten salt as HTF. Following conclusions were obtained: Nu increased firstly and then decreased when filling rate was increasing for both center filling and annular filling, and the optimal thermal performance were obtained when filling rate was 0.8 for center filling and 0.2 for annular filling. The circumferential temperature difference decreased firstly and increased when filling rate was increasing for both center types of filling and the lowest circumferential temperature difference were obtained at filling rate of 0.8 for center filling and 0.4 for annular filling. [14]

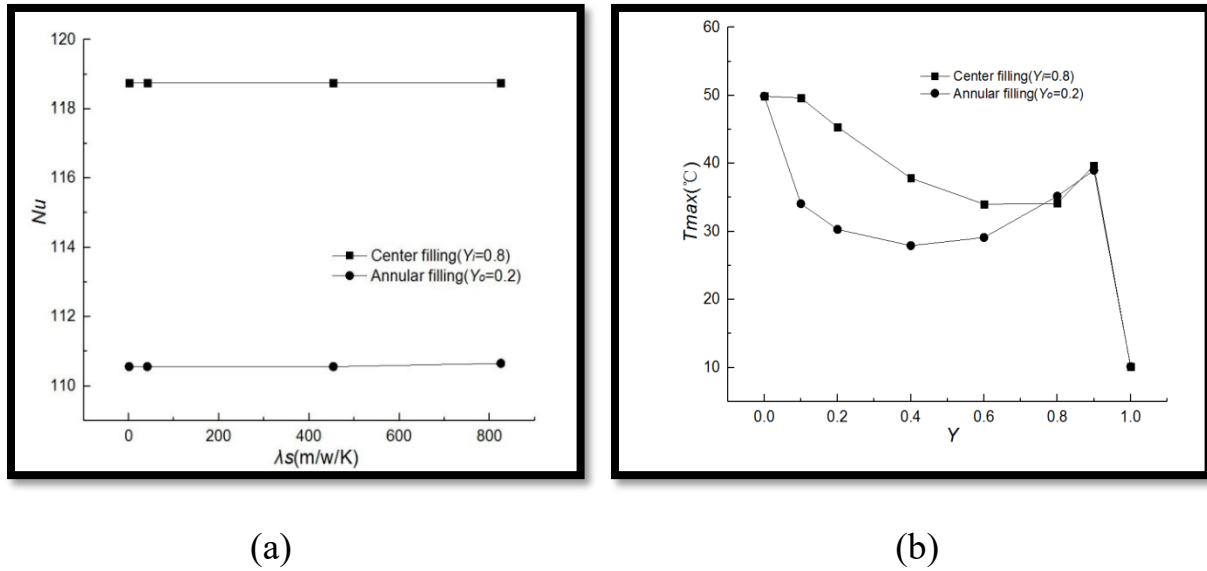


Figure 1.6 (a) The relationship of Nu and λ_0 for different kinds filling (b) The relationship of the maximum circumferential wall temperature difference of the tube and Y for different filling types

1.4 Purpose of Study

The goal of this research is to investigate the influence of Raschig rings on an absorber tube for a linear focusing solar thermal collector. This work will provide a complete overview of the thermal and dynamic characteristics concerning the receiver tube with porous medium. The procedures of this thesis are going to start with defining the geometry of the smooth pipe following the study of the optimized grid that has an important role to obtain accurate results. Grid optimization will be studied a smooth pipe and a half-pipe(symmetry) with two different types of fluid (water and Air) to guarantee the applicability of the grid for any types of the fluid, including air, water, and thermal oil. Finally, the effects of Raschig rings as a porous disc inserted in the center of an absorber tube heated with uniform heat flux distribution are compared with those of a smooth pipe.

CHAPTER TWO

CFD ANALYSIS AND SIMULATIONS SETUP

2.1 Geometry

Many possible configurations for absorber tube are found in the literature, so the geometry of pipe has been modified from literature. The first step required the tube geometry to be defined in STAR-CCM+®.

The general shape of an absorber tube inner, outer diameter with the specific length, in this work the geometry is defined 66mm an inner diameter, 70 mm an outer diameter and a length of 500 mm. Following, different physics were defined for respectively an internal cylinder as the fluid domain, an external cylinder as the solid domain, with an interface between. The stainless steel has been set as the material of the tube due to many advantages such as corrosion-resistant, withstanding high temperatures, and long-life span[15]. The glass plate and secondary reflector are not considered for simulations due to the complexity and the importance effect of transferring heat inside the tube. Cover tube is not included in this work due to uniform heat flux which does not consider losses in the tube such as radiation and convective respectively. Radiation losses mainly depend on the absorptivity and transmissivity factor.

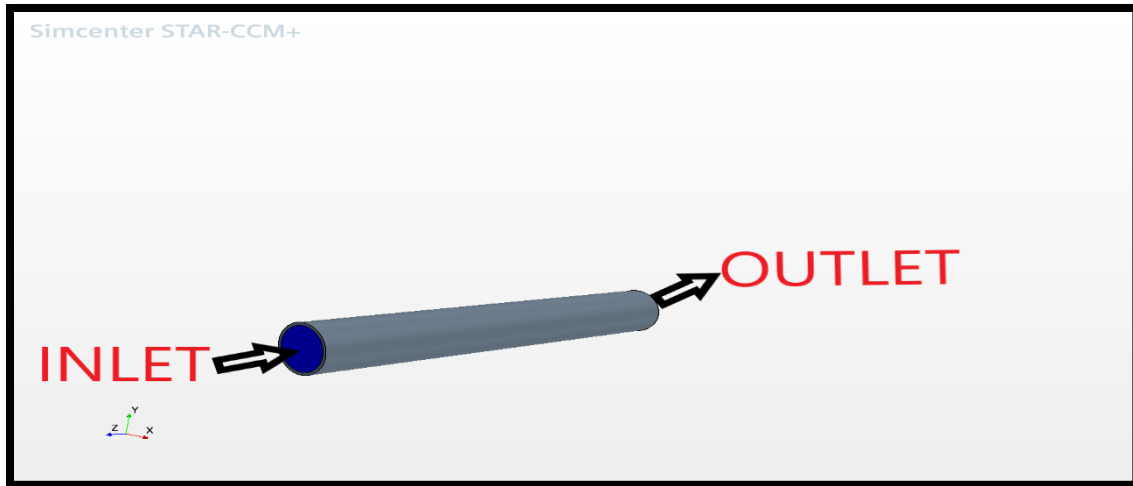


Figure 2.1 Geometry of smooth tube

2.2 Computational fluid dynamics

Computational fluid dynamics (CFD) is considered nowadays a powerful tool in the field of fluid flow problem solving. This method is based on the numerical solution of fluid flow equations with a discretization of the spatial domain. The most common approach to CFD analysis is the finite volume method: this method consists in the domain discretization into a finite set of control volumes where general conservation (transport) equations for mass, momentum, energy, species, etc. are solved. Partial differential equations are thus discretized into a system of algebraic equations solved numerically to obtain the global solution. [16]

The CFD resolution of a 3D problem using the commercial solver STAR-CCM+ is the basis for this thesis work.

As previously stated, any CFD approach is based on the discretization of a computational domain into sub-domains, resulting in the so-called mesh. A mesh is a collection of computational cells within which the CFD solver finds numerical solutions to flow equations. Different physics and geometry problems necessitate the use of different meshes capable of accurately describing each flow field. The total volume dimension is defined as the first mesh characteristic: the computational domain must be large enough to encase any fluid stream affected by the presence of solid bodies. [17]

A steady state RANS-type (Reynolds Averaged Navier-Stokes equations) model is adopted, as already implemented in STAR-CCM+ code. Turbulence is solved with a Shear-Stress Transport (SST) $k-\omega$ turbulence closure, a two-equation eddy-viscosity model able to describe both near-wall and a free-stream behavior. This specific choice is based on previous studied by Zanino[18] where the SST $k-\omega$ has been proven to well reproduce the turbulence problem with respect to experimental data.

2.3 Grid independence study

Every mesh is defined by a few variables; any change in one of these parameters results in a different mesh and, consequently, a different problem to be numerically solved. These parameters are cells number, cells dimensions, cells geometry, number of prism layers and prism layers thickness.

Richardson extrapolation uses two solutions on systematically refined grids to estimate the exact solution to the partial differential equations and is accurate only in the asymptotic range (i.e., when the grids are sufficiently fine). The uncertainty estimators are applied to local solution quantities to evaluate accuracy for all possible types of convergence rates.[19]

The numerical uncertainty is estimated with Grid Convergence Index (GCI) by the 5-step procedure, requiring running the simulation model while refining the grid (mesh). [20]

Step1: Define a representative cell, mesh, or grid size (h)

For three dimensional, structured, similar grids,

$$h = [(\Delta X_{max})(\Delta Y_{max})(\Delta Z_{max})]^{1/3} \quad (1)$$

For nonstructured grids,

$$h = [(\sum_{i=1}^N \Delta V_i)/N]^{1/3} \quad (2)$$

Step 2: Select three grids with different resolutions and run simulations to determine the values of key variables

Grid refinement:

$$r = \frac{h_{coarse}}{h_{fine}} > 1.3 \quad (3)$$

Step 3: let $h_1 < h_2 < h_3$ and $r_{21} = h_2/h_1$, $r_{32} = h_3/h_2$

Calculate the apparent (observed) order, p , of the method,

$$p = \left[\frac{1}{\ln(r_{21})} \right] \left[\ln \left| \frac{\varepsilon_{32}}{\varepsilon_{21}} \right| + q(p) \right] \quad (4)$$

$$q(p) = \ln \left(\frac{r_{21}^p - s}{r_{32}^p - s} \right) \quad (5)$$

$$s = 1 * \text{sign} \left(\frac{\varepsilon_{32}}{\varepsilon_{21}} \right) \quad (6)$$

Where $\varepsilon_{32} = \varphi_3 - \varphi_2$, $\varepsilon_{21} = \varphi_2 - \varphi_1$, and φ_k denotes the simulation value of the variable on the k^{th} grid. In our simulations pressure drops and outlet temperature are considered.

Step 4: Calculate the extrapolated values:

$$\varphi_{ext}^{21} = \frac{(r_{21}^p \varphi_1 - \varphi_2)}{(r_{21}^p - 1)} \quad (7)$$

Step 5: Calculate error estimates

$$e_a^{21} = |\varphi_1 - \varphi_2| \quad (8)$$

Then the Grid Convergence Index (GCI) is

$$GCI_{fine}^{21} = \frac{F_s * e_a^{21}}{r_{21}^p - 1} \quad (9)$$

The investigation was based on three kinds of grids coarse, medium, and fine for turbulent flow and $k-\omega$ SST type of model to study the effect close the wall. Under the same initiation the convergence process determined by the pressure drops (Δp) for fluid dynamic and the outlet temperature (T_{out}) of a receiver for thermal study. The accurate numerical simulation of pressure drops and temperature distribution in STAR-CCM+® depended greatly on the simulation setup.

The coarse grid consists of 6 prism layers with base size of 4mm, while the medium grid is 8 prism layers with 2mm base size, and the finer mesh has chosen 10 prism layers with 0.9mm base size.

2.4 Simulation setup

This section considered two scenarios, the first scenario is full pipe, and the second scenario is half-pipe (symmetry) using Air and water as fluid to have confidence that the grid is suitable for any scenarios under any kinds of fluid.

The flow parameters used as constant function of temperature such as density, thermal conductivity and specific heat and dynamic viscosity, On the solid part of the receiver, a uniform heat flux applied in CFD. The fluid part is divided into three regions inlet, outlet, and wall, in the solid part the regions are inner wall, outer wall, inlet side and outlet side. These parts are used in the defining the boundary conditions. The interfaces are done between inlet and outlet and between the wall of fluid part and inner wall of solid part for most of simulations the fully developed interface is applied. The mass flow is constant for all simulations 0.15 kg/s and in this section.

Inner diameter	66mm
Outer diameter	70mm
Length of pipe	500mm
Mass flow	0.15 kg/s
Type of model	$k-\omega$ SST
Inlet temperature	20 °C
Type of flow	Turbulent
Heat flux	50000 w/m ²
Heat transfer model	Conjugate heat transfer

Table 2.1 simulation parameters

2.4.1 Hydraulics

CFD mesh structure is very complex issue and always more than one solution is possible depending on the problem requirements. In this study, the simulations are run isothermally, setting the boundary conditions as fully developed for all scenarios and types of fluid under the assumption of the inlet temperature of 20 °C for water and air. It is critical to emphasize how mesh optimization is typically required for any CFD problem. In overall, many cells, if properly shaped and sized, will be able to better describe the flow problem, but will take longer to solve. The simulation runs till it gets converged for pressure drop and mass flow by showing asymptotic feature, the three grids have the same surface growth rate and mesh type which is polygonal but mainly differences are number of prism layers, total number of cells, and prism layer near wall thickness. Y^+ is the most important value to be considered as ~ 1 to comply with low y^+ wall treatment and the viscous sublayer region

The total volume domain only includes the fluid part in comparison with thermal model the total volume consists of two parts fluid and solid.

2.4.1.1 Full pipe Air

In the method explains previously of computing Richardson extrapolation to obtain a converged result the presented table and figure below, the optimum result of pressure drops for the number of prism layers 10 and 0.9mm base size with total number of cells 66040.

No. prism layers	10	8	6		
Base size(mm)	0.9	2	4		
Number of cells	66040	17000	5470		
Average element size(mm)	2.84	4.46	6.51		Total volume domain(mm ³)
Pressure drop (pa)	129.98	128.84	125.63		1.51E+06
	h1	h2	h3		
Refinement ratio	r21	1.57	r32	1.46	
Order of convergence	2.29				
ea21	8.77E-03				
GCI	0.60%				
Richardson	130.61				
Error21	0.88%				
Error32	2.49%				

Table 1.2 The calculation results for pressure drop in different grides for full pipe Air

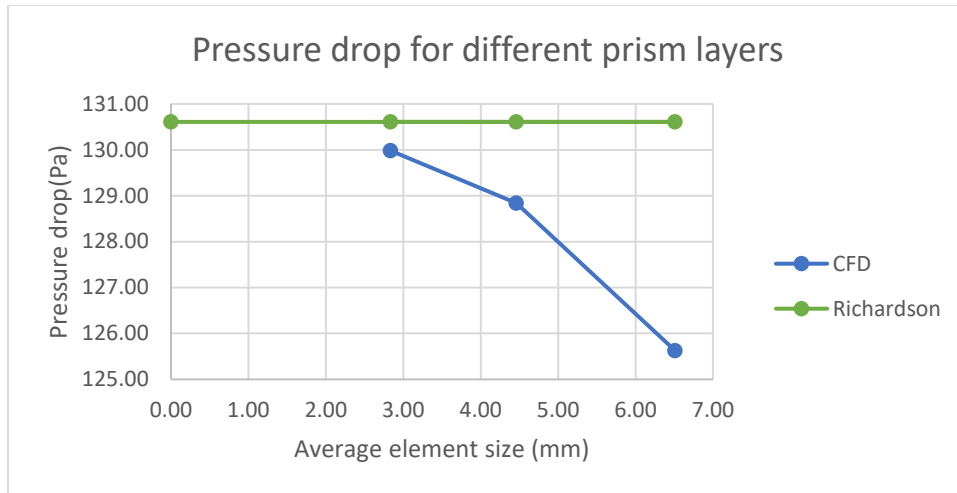
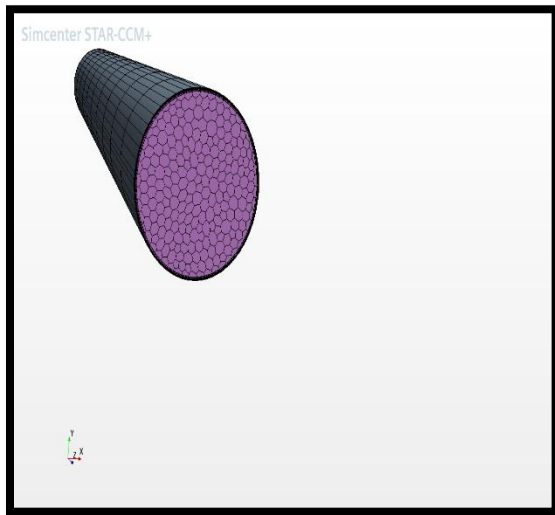
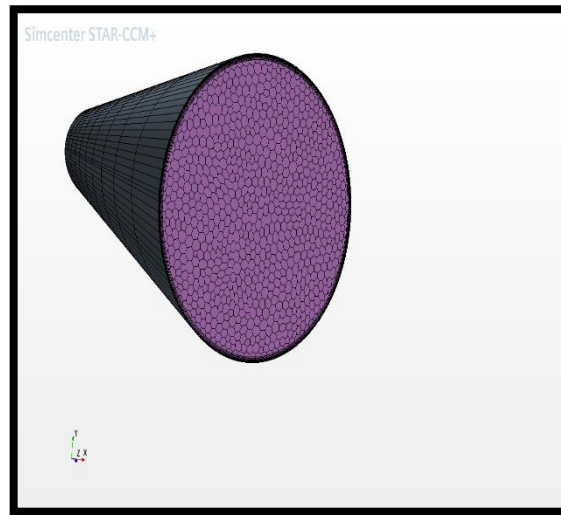


Figure 2.2 Pressure drop using Richardson for full pipe Air

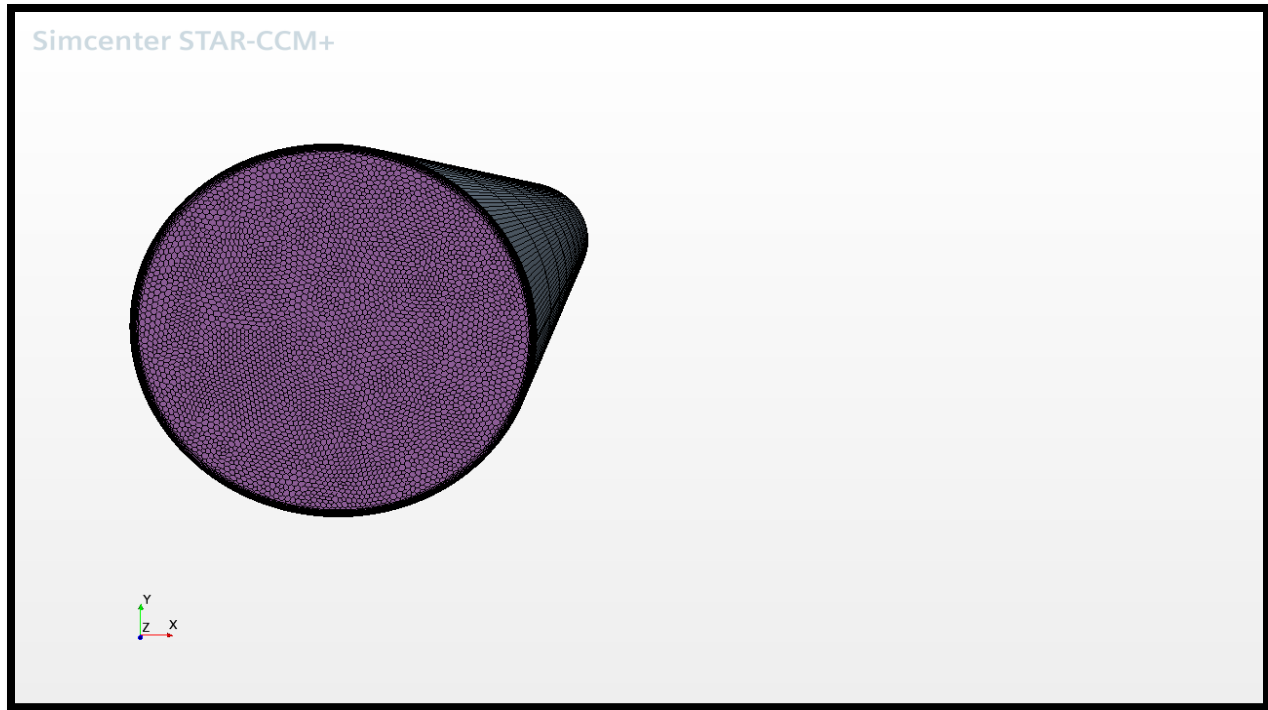
The CFD values obtained after many numbers of iterations depending on the convergence and the residuals of continuity and momentum equations, the error is around 0.88% which is an acceptable value.



(a)



(b)



(c)

Figure 2.3 Three different grids (a) coarse (b) medium (c) fine for full pipe

2.4.1.2 Full pipe water

The same procedures are done in this section, but the only difference is the type of fluid, as matter of fact the pressure drop has small values compared with air due to compressibility effect, as the result obtained it is found that 10 prism layers with 0.9 mm base size most suitable value close to Richardson extrapolation.

No. prism layers	10	8	6		
Base size(mm)	0.9	2	4		
Number of cells	66040	17000	5470		
Average element size(mm)	2.84	4.46	6.51		Total volume domain(mm ³)
Pressure drop(pa)	0.66	0.65	0.63		1.51E+06
	h1	h2	h3		
Refinement ratio	r21	1.57	r32	1.46	
Order of convergence		2.87			
ea21		0.01			
GCI		0.41%			
Richardson		0.66			
Error21		0.88%			
Error32		3.26%			

Table 2. 2 The calculation results for pressure drop in different grides for full pipe water

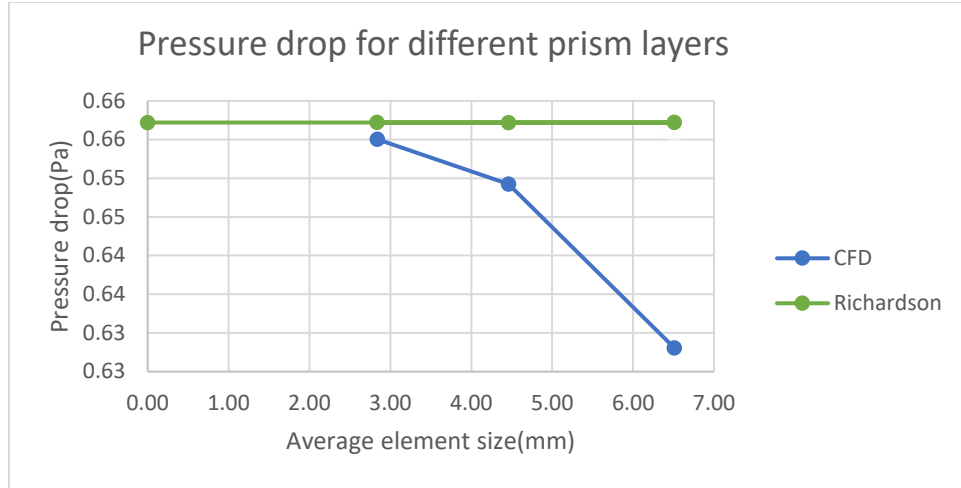


Figure 2.4 Pressure drop using Richardson for full pipe water

The Richardson extrapolation is a method for obtaining a higher-order estimate of the continuum value (value at zero grid spacing) from a series of lower-order discrete values. In the results above Richardson has a linear behavior to comply with convergence results from CFD.

2.4.1.3 Half pipe Air

The boundary conditions for the bottom side of half pipe are considered as symmetry, and the remaining parts are same as pervious simulations, the number of total domain volume has decreased due to the geometry design, thus the number of cells and pressure drops result changed.

No. prism layers	10	8	6		
Base size(mm)	0.9	2	4		
Number of cells	36970	9470	3040		
Average element size(mm)	2.85	4.49	6.55		Total volume domain(mm ³)
Pressure drop(pa)	381.72	363.29	358.09		8.55E+05
	h1	h2	h3		
Refinement ratio	r21	1.57	r32	1.46	
Order of convergence	2.79				
ea21	0.05				
GCI	2.37%				
Richardson	388.97				
Error21	4.83%				
Error32	1.43%				

Table 2.3 The calculation results for pressure drop in different grides for half pipe Air

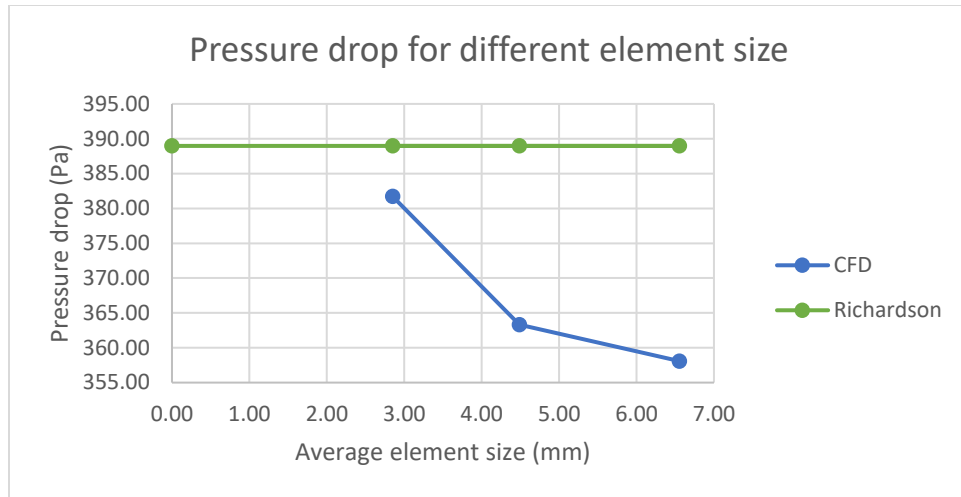
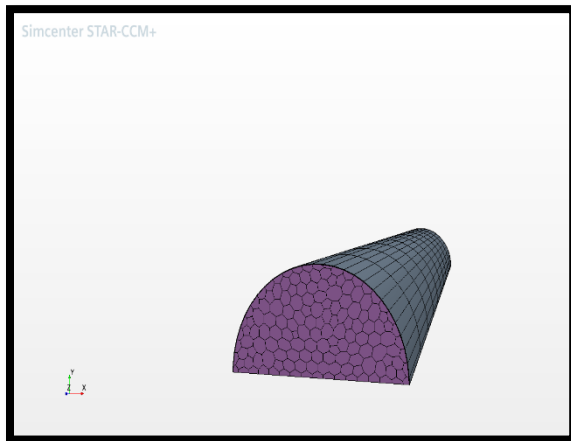
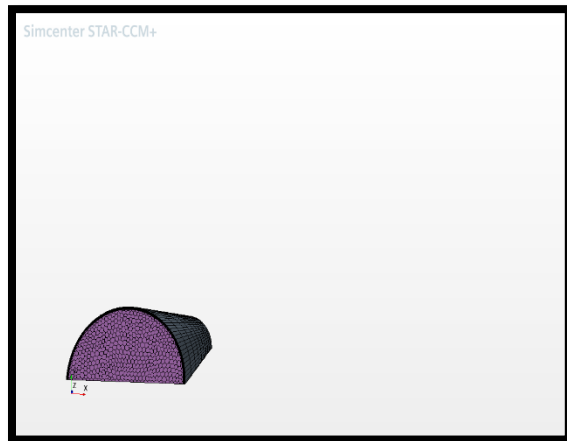


Figure 2.5 Pressure drop using Richardson for half pipe Air

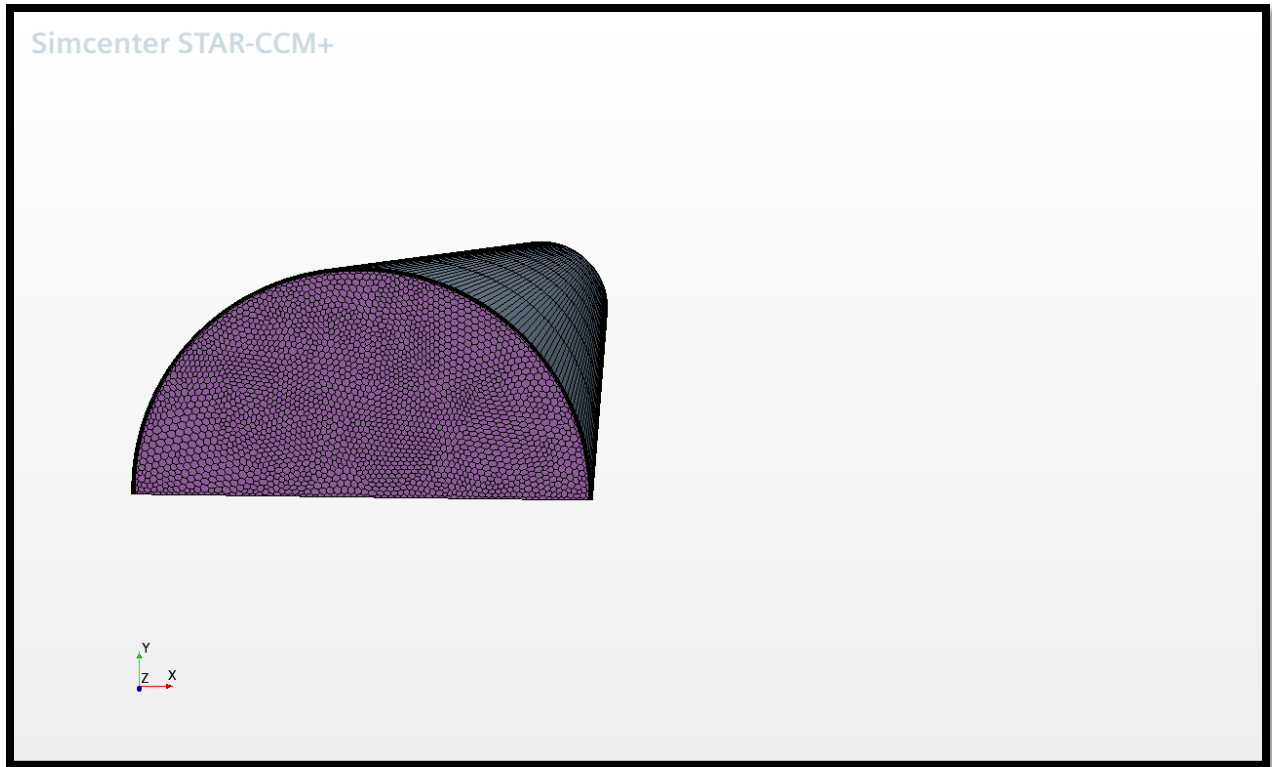
The ideal gas properties are giving at constant temperature 20 °C and the simulations run till the convergence, the error increased to 4.83% for the fine grid in comparison with full pipe the reason beyond this effect is due to geometry of tube as mentioned, the optimum mesh depends on the geometry of the domain.



(a)



(b)



(C)

Figure 2.6 Three different grids (a) coarse (b) medium (c) fine for half pipe

2.4.1.4 Half pipe water

Boundary value problems are extremely important as they model a vast number of phenomena and applications, from solid mechanics to heat transfer, from fluid mechanics to acoustic diffusion. They arise naturally in every problem based on a differential equation to be solved in space, while initial value problems usually refer to problems to be solved in time. [21]

The similar boundary conditions applied, only using water instead of air in the defining of physics the results of geometry and number of cells do not change.

No. prism layers	10	8	6		
Base size(mm)	0.9	2	4		
Number of cells	36970	9470	3040		
Average element size(mm)	2.89	4.47	6.50		Total volume domain(mm ³)
Pressure drop(pa)	1.75	1.11	1.09		8.55E+05
	h1	h2	h3		
Refinement ratio	r21	1.55	r32	1.46	
Order of convergence	7.43				
ea21	0.36				
GCI	1.85%				
Richardson	1.77				
Error21	36.36%				
Error32	2.24%				

Table 2.4 The calculation results for pressure drop in different grides for half pipe water

Care must always be taken in determine the appropriate grid resolution problem to minimally resolve the physics problem. The error obtained in this simulation is very high for the fine grid thus, it could be a coarse grid an adequate to resolve the pressure drop problem.

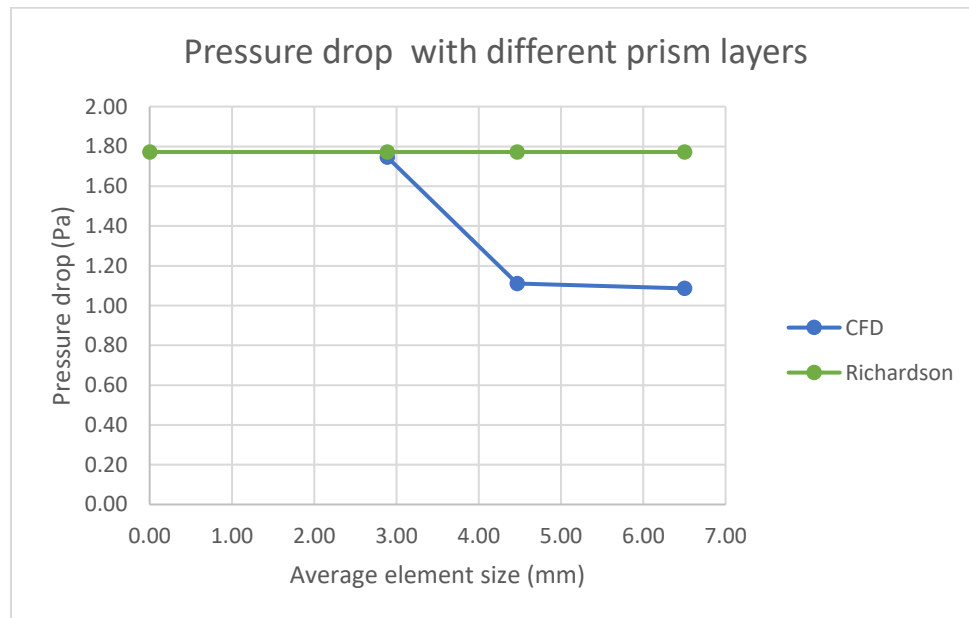


Figure 7 Pressure drops using Richardson for half pipe water

After all , the fine grid has a close value with Richardson ,but the main problem is the error obtined could affect the level of accuracy that intended to reach .

2.4.2 Thermal study

In this model the physics are divided into solid domain which a uniform heat flux applied with amount of 50000 w/m^2 and fluid domain a segregated fluid temperature used instead of isothermal fluid. Solid domain for external tube and fluid domain for internal tube for defining the regions to apply the boundary conditions simply. Solar radiation was assumed to be the same amount of heat flux and neglecting all losses the absorbed heat calculated by multiplying this heat flux for the surface area of pipe and half pipe. Then heat equation used to obtain the temperature differences between inlet and outlet. All flow parameters such as thermal conductivity, specific heat, density, and dynamic viscosity are taken at inlet temperature. In the solid part the material defined with constant parameters. Moreover, the segregated solid energy considered to have the interface between solid and fluid part.

$$A_s = \pi * D_o * l \quad (10)$$

$$Q = q * A_s \quad (11)$$

$$Q = m \cdot cp * \Delta T \quad (12)$$

2.4.2.1 Full pipe Air

The aim of this study to obtain higher outlet temperature to improve the thermal performance of the receiver, thus the simulations run with the ideal gas properties under the constant values, the results represented in table and figure below, the amount of outlet temperature has higher value in medium grid, but it is still far from Richardson extrapolation.

No. prism layers	10	8	6		
Base size(mm)	0.9	2	4		
Number of cells	82340	20680	14580		
Average element size(mm)	2.64	4.18	4.69		Total volume domain(mm ³)
Outlet temperature	386.77	387.04	386.89		1.51E+06
	h1	h2	h3		
Refinement ratio	r21	1.58	r32	1.12	
Order of convergence	1.32				
ea21	0.07%				
GCI	0.10%				
Richardson	386.44				
Error21	0.07%				
Error32	0.04%				
Inlet temperature(K)	350.20	350.43	350.29		
Outlet temperature(K)	386.77	387.04	386.89		
Temperature of wall(K)	793.12	798.70	798.67		
Temperature of fluid(K)	366.68	366.99	366.87		
$\Delta T(K)$	36.56	36.60	36.61		

Table 2.5 The calculation results for temperatures in different grides for full pipe Air

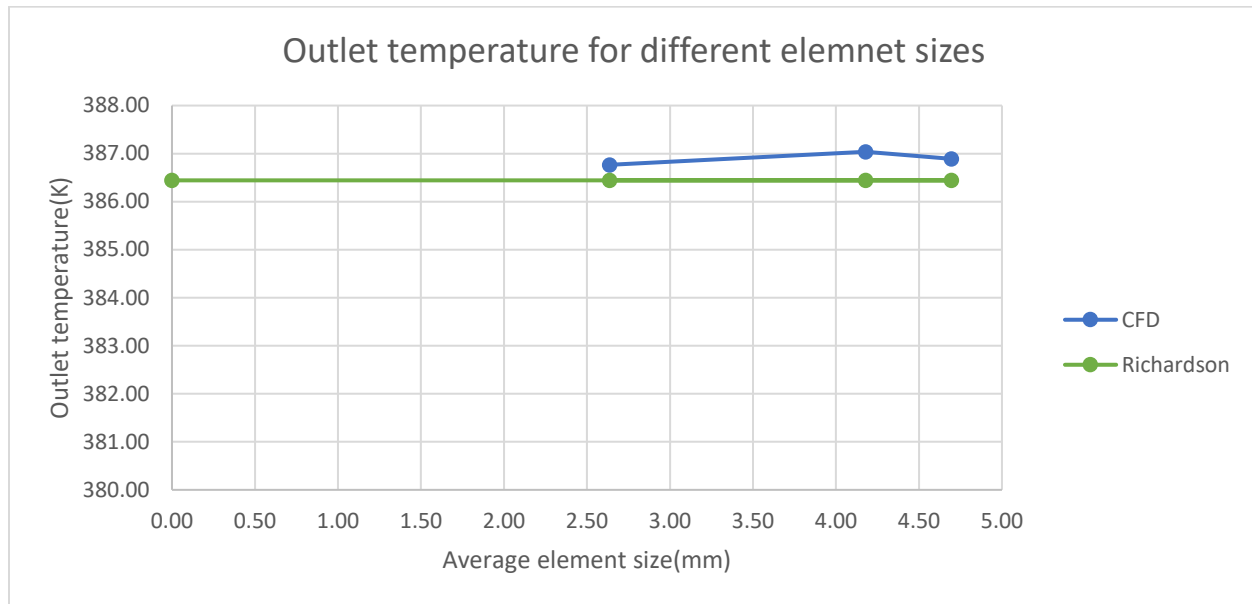


Figure 2.8 Outlet temperature using Richardson for full pipe Air

The temperature of fluid for all the grids are similar but the only differences are the temperatures of wall which have a major effect of absorbing energy from the sun. The optimum grid for this study is medium grid but it has higher error than fine grid therefore the fine grid is considered.

2.4.2.1 Full pipe water

Similar processes are done in the section, in fact the heat capacity of water has higher value in comparing with air thus, the outlet temperatures of grids have higher value. In contrast, the differences between inlet and outlet temperature are very low for water due to same reason.

No. prism layers	10	8	6		
Base size(mm)	0.9	2	4		
Number of cells	82340	20680	14580		
Average element size(mm)	2.64	4.18	4.69		Total volume domain(mm^3)
Outlet temperature	403.30	405.33	406.12		1.51E+06
	h1	h2	h3		
Refinement ratio	r21	1.58	r32	1.12	
Order of convergence	2.04				
ea21	0.50%				
GCI	0.40%				
Richardson	402.00				
Error21	0.50%				
Error32	0.20%				
Inlet temperature(k)	394.57	396.56	397.37		
Outlet temperature(K)	403.30	405.33	406.12		
Temperature of wall(K)	777.46	780.01	789.33		
Temperature of fluid(K)	398.56	399.66	401.31		
$\Delta T(K)$	8.72	8.76	8.75		

Table 2.6 The calculation results for temperatures in different grides for full pipe water

The best result obtained from the coarse grid in term of outlet temperature, temperature of wall and temperature of fluid, in addition of error it reached small error around 0.2%.

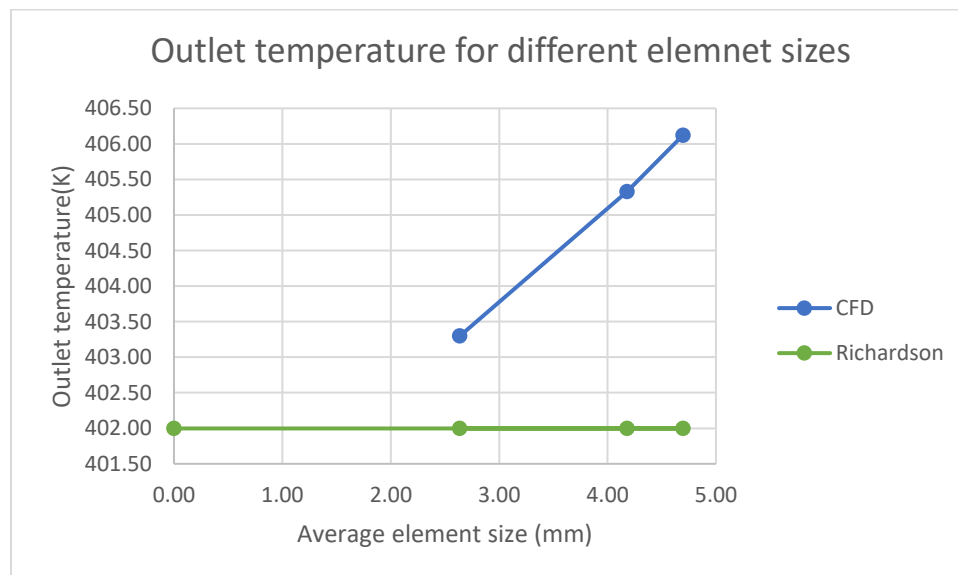


Figure 8 Outlet temperature using Richardson for full pipe water

The three grids run differently and the time of running the simulations to be converged are different because the fine grid takes longer time.

2.4.2.3 Half pipe Air

The surface area of pipe divided by two in the equation (10) and the mesh is done along the longitudinal of pipe with chosen number of layers of 50 in volume distribution to increase the number of cells at the end of simulation, in the previous simulations for full pipe the number of layers is 10. These are main differences between two geometries.

The surface control allows to custom the prism layers only on the fluid part, and target surface size in fluid domain to 1.5 mm.

No. prism layers	10	8	6		
Base size(mm)	0.9	2	4		
Number of cells	202400	102400	81050		
Average element size(mm)	1.62	2.03	2.19		Total volume domain(mm ³)
Outlet temperature	344.95	345.11	345.61		8.55E+05
	h1	h2	h3		
Refinement ratio	r21	1.25	r32	1.08	
Order of convergence	4.97				
ea21	0.05%				
GCI	0.03%				
Richardson	344.87				
Error21	0.05%				
Error32	0.15%				
Inlet temperature(k)	326.42	326.60	327.11		
Outlet temperature(k)	344.95	345.11	345.61		
Temperature of wall(k)	611.63	615.65	625.24		
Temperature of fluid(k)	335.59	336.05	336.18		
$\Delta T(K)$	18.53	18.51	18.50		

Table 2.7 The calculation results for temperatures in different grides for half pipe Air

The fine grid has 0.05 % error while the medium reached 0.15%, thus the optimized grid to be considered for simulation is fine grid, besides lower value of outlet temperature.

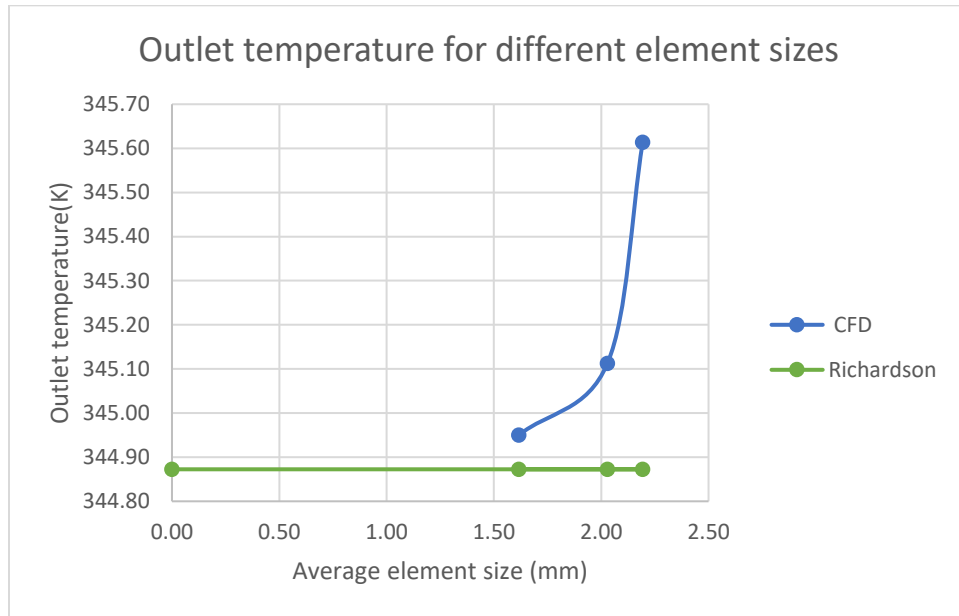


Figure 2.10 Outlet temperature using Richardson for half pipe Air

The simulations of CFD enable the maximum steps of stopping criteria to be defined as mentioned in the previous model this has to be running until the results have a linear behaviour of outlet temperature. The average element size depends on the total volume domain and number of cells thus the average element size diminished to half.

2.4.2.4 Half pipe water

The boundary conditions are fully developed for flow and energy, the two options are mass flow and constant heat flux walls with the defined minimum inflow temperature instead of bulk mean inflow temperature which is going to be applied in the simulations setup of chapter four. The results have similar manner of full pipe of water for the optimized grid.

No. prism layers	10	8	6		
Base size(mm)	0.9	2	4		
Number of cells	39580	20120	15800		
Average element size(mm)	2.78	3.49	3.78		Total volume domain(mm ³)
Outlet temperature	354.28	354.34	355.09		8.55E+05
	h1	h2	h3		
Refinement ratio	r21	1.25	r32	1.08	
Order of convergence	11.80				
ea21	0.01%				
GCI	0.0013%				
Richardson	354.28				
Error21	0.01%				
Error32	0.21%				
Inlet temperature (K)	349.91	349.95	350.71		
Outlet temperature (K)	354.28	354.34	355.09		
Temperature of wall (K)	597.69	598.40	604.59		
Temperature of fluid (K)	351.94	351.93	352.69		
ΔT (K)	4.38	4.38	4.38		

Table 2.8 The calculation results for temperatures in different grides for half pipe water

The order of convergence in this simulations reached higher value 11.8, On the other hand , GCI has lowest value among all other studies . The computed outlet temperature of fine grid has the same value obtained in Richarson .

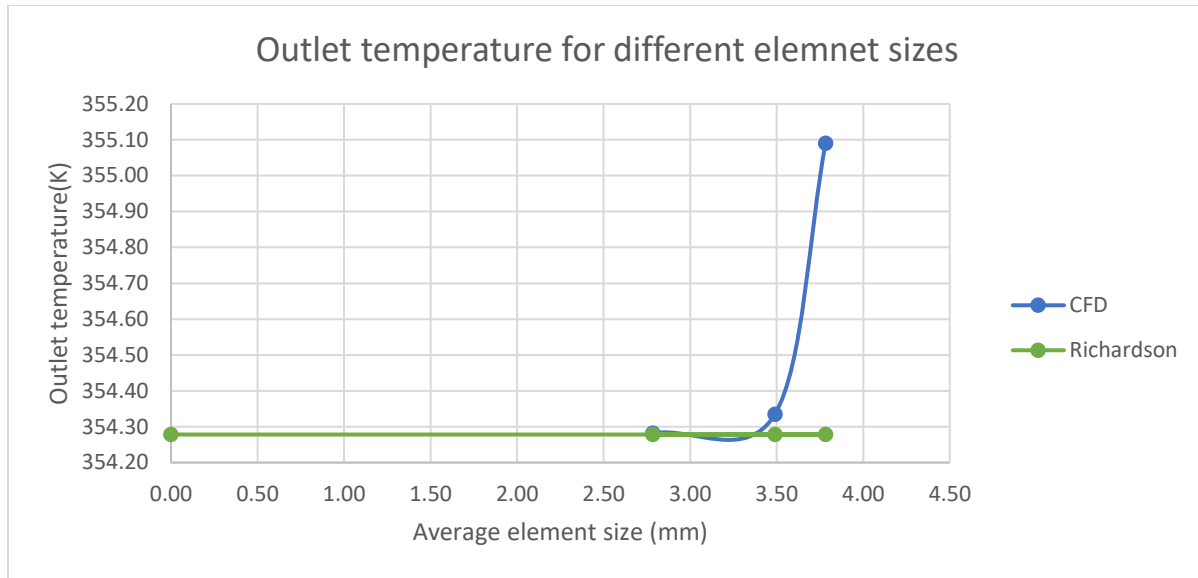


Figure 2.11 Outlet temperature using Richardson for half pipe water

At the end of these studies , it ended up that these results give logical reasons to chose the optimum mesh for the comparison between smooth tube and tube with Raschig rings that will be discussed in the last chapter. The fine grid achieves the simulation objectives for esitimated accuracy.

2.5 Preliminary Validation

In this section, thermal oil is going to be used instead of the other two types of fluid to validate the literature with a reference study. [11] The parameters of thermal oil such as density, dynamic viscosity, thermal conductivity, and specific heat have been extracted from the graphs and then used as polynomial function of temperature. The range of temperature is between 323 and 623 k.

The validation process starts using the optimized grid of 10 prism layers and base size of 0.9mm for the pipe with 12 m length, 66 mm inlet diameter, and 70 mm outside diameter. The turbulent model used is $k-\omega$ SST because this model gives better result near the wall, for inlet temperature 600k with flow rate equals to 150 L/min.

Two boundary conditions are applied, where the first concerns developed interface, while the second assumes the inlet velocity and outlet pressure with 15 bar to keep the working fluid in a liquid phase.

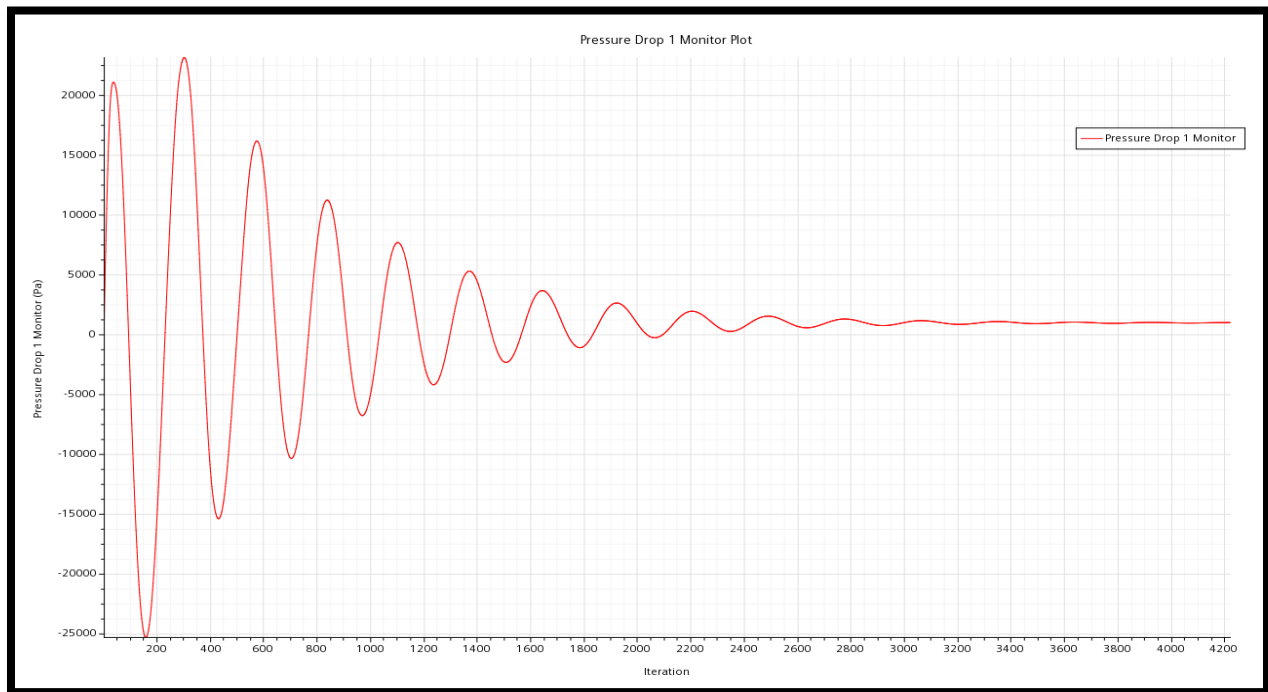
$$f = \frac{\Delta p * D_i}{\frac{1}{2} * \rho * u^2 * l} \quad (13)$$

$$f_{th} = \frac{0.184}{Re^{0.2}} \quad (14)$$

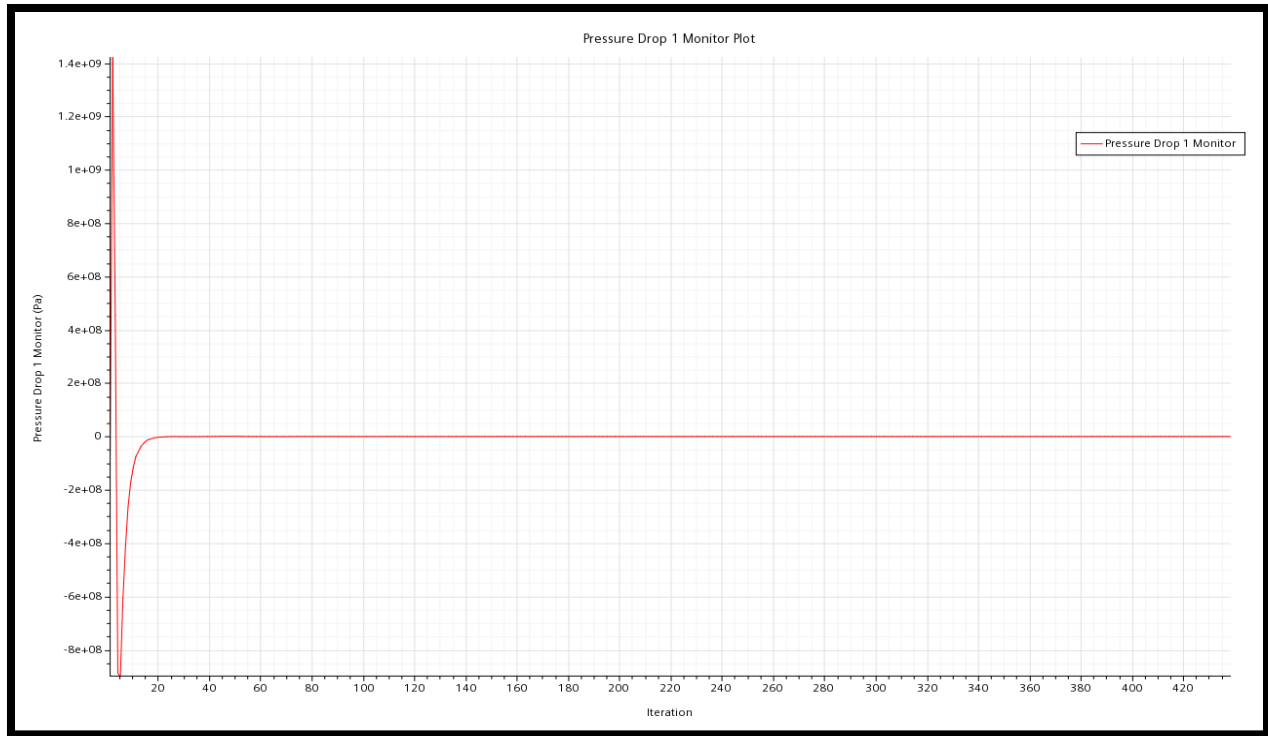
Boundary conditions	Reference study	developed interface	Inlet velocity & outlet pressure
Pressure drops (Pa)	600	573.66	601.49
Error %	-	4.39%	0.24%

Table 2.9 validation results

The result obtained at the second assumption of boundary conditions have close agreement with reference study, this boundary specifies to have liquid phase at the outlet, on the other side, the fully developed can be applied in the next simulations because the fluid is gas and there no need to have liquid phase.



(a)



(b)

Figure 2.12 pressure drop convergence in (a) fully developed and (b) inlet velocity boundary conditions

These results explain the number of iterations for the two types of boundary conditions, the running time of developed interface takes longer time to get converged than the inlet velocity and outlet pressure.

At the end of this study, it is clearly seen that the optimized grid is going to be applied in all simulations is a fine mesh with 10 prism layers and 0.9 mm base size, as mentioned previously y^+ is ~ 1 to comply with viscous sub-layer region only considering for comparison air with a half-pipe for hydraulic and thermal study seen in figure (13,14).

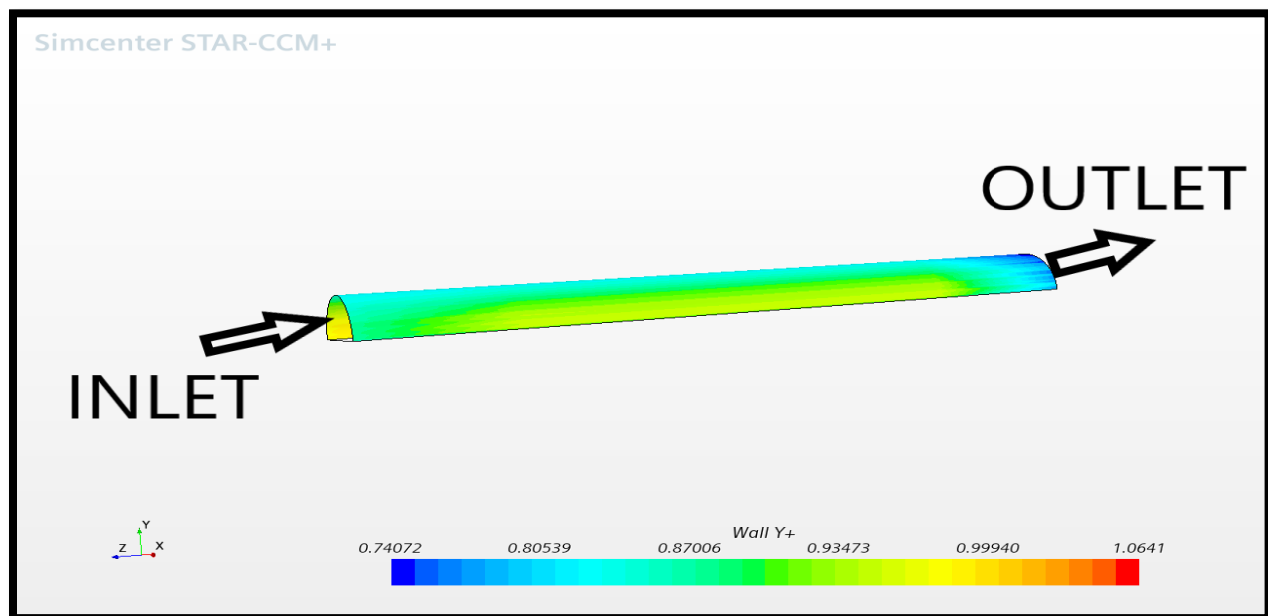


Figure 2.13 Y+ value for the wall under dynamic behavior

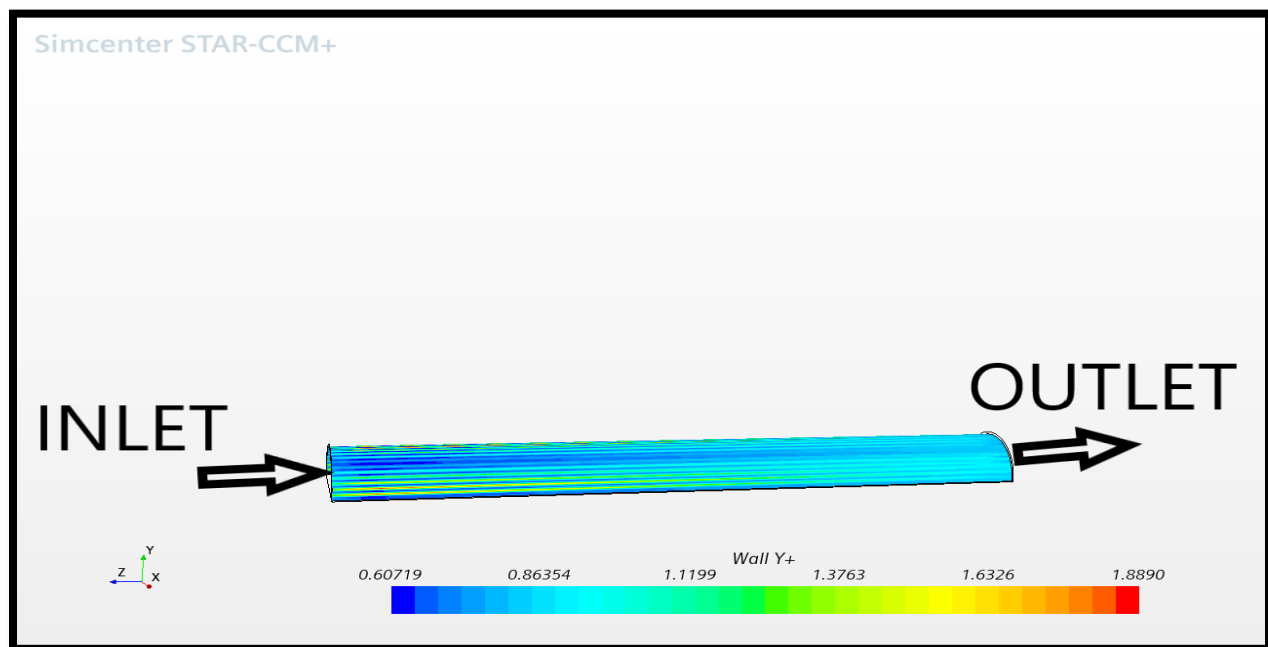


Figure 2.14 Y+ value for the wall under heat flux

CHAPTER THREE

RASCHIG RINGS POROUS MEDIUM

3.1 Overview of Raschig rings

Porous media comprise extremely complicated flow paths, and thus cause pressure drops when they are connected in a circuit. Therefore, an accurate prediction of the pressure drop is crucially needed for performance evaluation. Several studies have demonstrated the physics of flow through porous media under the assumption that the internal structure is isotropic and homogeneous. Their findings show that the Darcy regime can predict flow behavior properly when the flow is dominated by viscous effect.[22]

In catalytic processes where liquid is present, the catalyst pores are likely to be filled with the liquid and low diffusivity in the liquid phase may even increase the likelihood of diffusion limitation. In the case of porous solid catalysts, by far the largest portion of catalytically active surface area consists of pore walls. For a given conversion rate, the external surface determines the flux density for diffusion of reactants to the catalytic surface inside the volume of catalyst particle.[23]

The effectiveness of the rings is a function, not only of their shape, which determines the packing efficiency as well as the packing surface area but also, of the material properties such as porosity and specific surface area.[24]

A way of enhancing the convective heat transfer from the wall to the fluid, alternative to any attempt to increase directly the HTC, is to insert a porous medium under the irradiated surface. Porous media are widely applied in industry to enhance the heat transfer rate from catalyst carriers in chemistry, thermal exchange in electrical cooling, thermal insulation in buildings and astronautics,

low emission combustion technologies and receivers for concentrating solar power.[10]

3.2 Simulation part

Three-dimensional computational fluid dynamics (CFD) simulations with discrete particles resolved have been extensively developed for the past twenty years. Many efforts have been made to put forward the application of this approach. The computer-generated random packing of spherical and non-spherical particles is realized either by Discrete Element Methods (DEM) or Monte-Carlo methods.[25]

With the increase of computational power in the last years it is possible to use CFD for simulating spatially resolved fixed bed reactors. For such a CFD simulation a 3D structure of the fixed bed is needed, and this structure must be subdivided in small control volumes, this means it has to be meshed.[26]

In this work the only fluid is going to be used is air under the assumption of turbulent flow, Turbulence is solved with a Shear-Stress Transport (SST) $k-\epsilon$ Realizable model is turbulence closure, a two-equation eddy-viscosity model able to describe the free shear flow behavior.

The simulations start isothermally using three different mass flow 0.025 ,0.03 and 0.04 kg/s respectively, similar boundary conditions applied fully developed interfaces these CFD simulations stop when they have an asymptotic feature of pressure drop and mass flows and outlet temperature for thermal model, it is noticed that when applying a uniform heat flux, the iterations take long time to get converged for energy equations.

The total domain consists of two parts solid and fluid, the heat flux applied to solid part with amount of 50000 W/m^2 with segregated solid energy and segregated fluid temperature.

The mesh for the simulations is a polyhedral cells-based mesh with around 7.3 million of cells. After the same procedures of grid independence study in the second chapter for optimized mesh ,5 prism layers with a 1.2 mm base size were applied while, the base size used for Raschig rings region was 0.2.

Number of cells	Faces	Vertices
7.3 million	35 million	26 million

Table 10 Mesh result of tube with Raschig rings

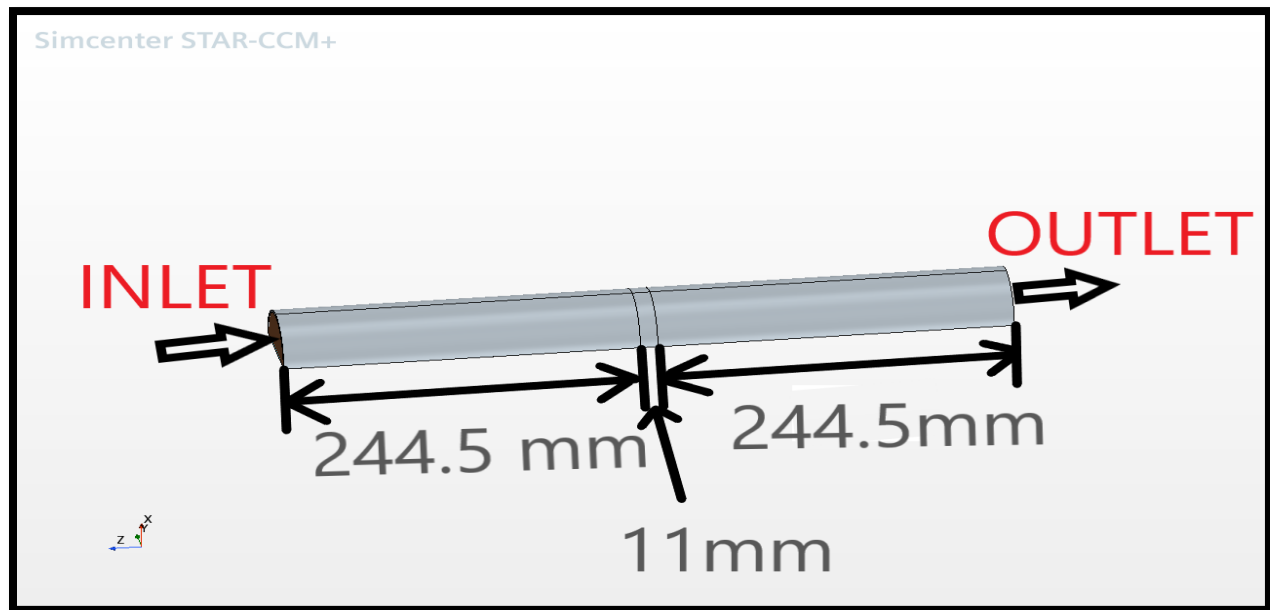


Figure 9 Geometry of the tube with Raschig rings

The Raschig rings inserted in the center of tube, so inlet and outlet have the same length 244.5 mm and the section of Raschig rings has 11 mm. Moreover, in the simulation setup the compound tube divided to upper and lower part for simplicity of applying the boundary conditions.

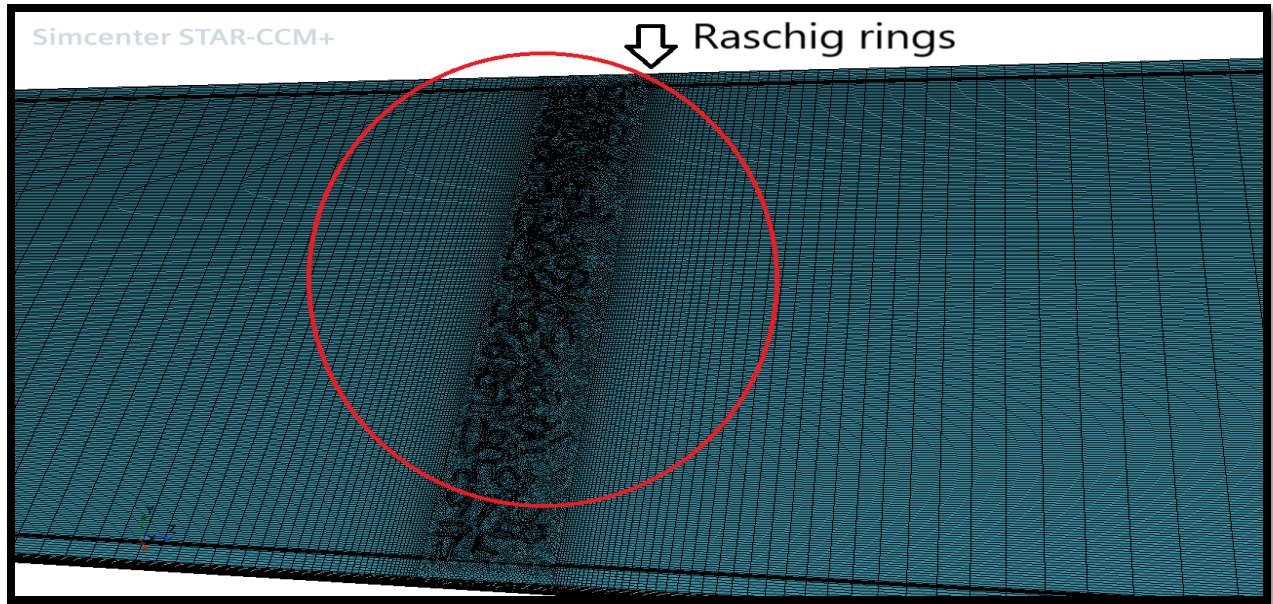


Figure 10 Mesh of tube with RRs on the bottom side

The number of layers extruded in a longitudinal of tube is 50 for both sides inlet and outlet to have a greater number of cells while in Raschig rings region these number increased to more than 100 layers.

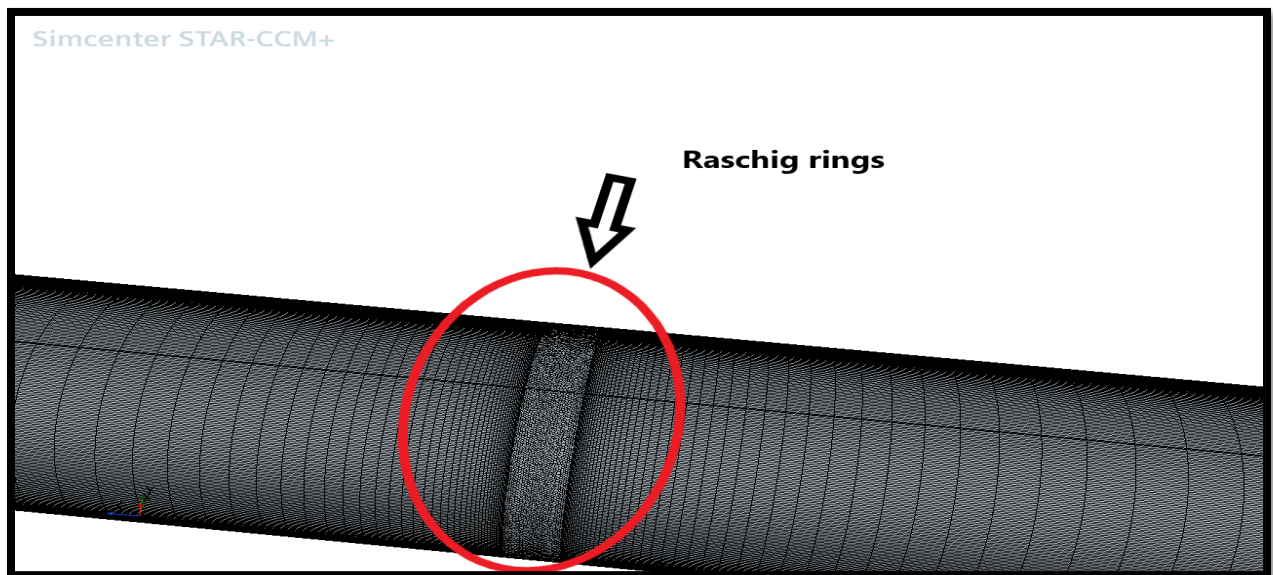


Figure 11 Mesh of tube with RRs on the bottom side

The shape of Raschig rings is cylindrical, consists of external diameter, thickness, and the height. There are many geometries of rings to be chosen but the precise dimension of the rings cannot be disclosed.

Chapter four

Results

This chapter gives a complete comparison between smooth tube and an enhanced tube in terms of fluid dynamic and thermal effects.

The simulations of hydraulic part only applied to fluid domain as mentioned previously the best way to study the inflow inside the tube for turbulent model is $k-\epsilon$ Realizable (ref) these setups considered for both tubes. The polynomial function of temperature used for flow parameters in the range of temperature 323 to 623 K, like thermal oil that was done in the second chapter. The inlet temperature is considered the ambient temperature of air which is 300K.

In the thermal effect a uniform heat flux applied as DNI (Direct nominal irradiance) assuming all losses are negligible, for energy developed interface, it is recommended to apply bulk mean inflow temperature to reach the average temperature of fluid inside the tubes. The regions are defined as previously which was discussed in the second chapter.

4.1 Hydraulic characteristics

Pure hydraulic analysis is done to investigate the pressure drop happens for smooth tube and tube with Raschig rings then it follows thermal test to find out the major effect of Raschig rings. To figure out the hydraulic characteristic of tube, the simulations are run isothermally for three different mass flow rates which produce different Reynolds numbers and various friction factor can be calculated on correlations applied in the validation process section.

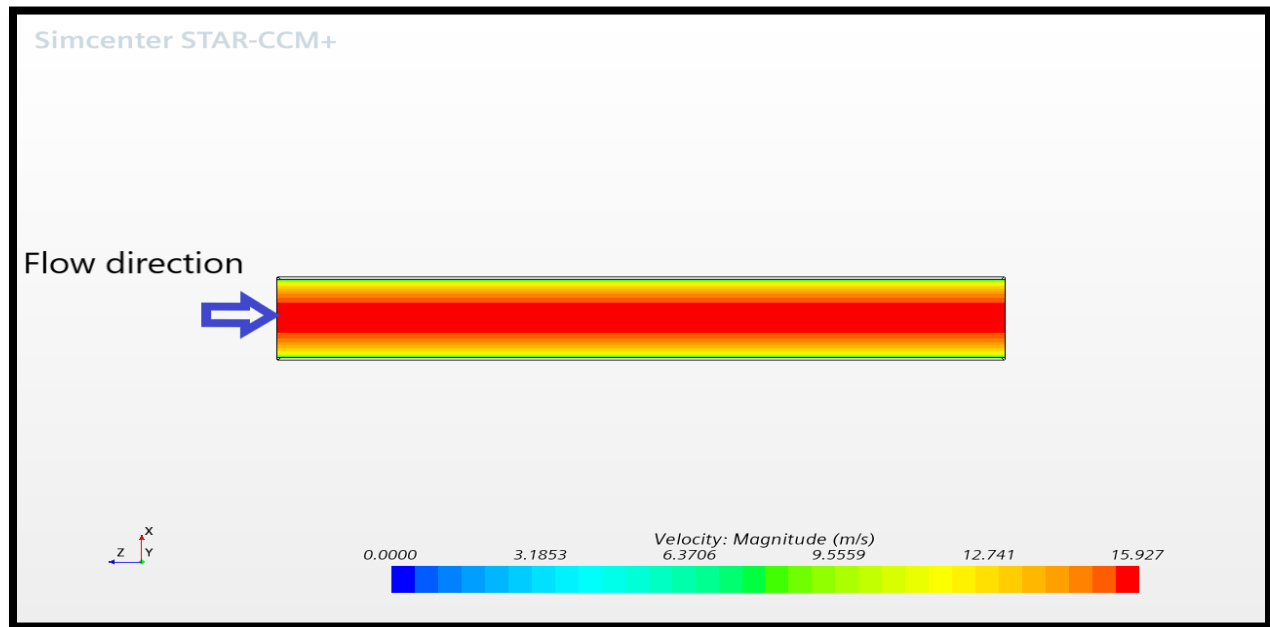
4.1.1 Smooth tube

The geometry of this tube is half pipe with similar dimension of previous studies, three different simulations obtained after applying mass flow of 0.025, 0.03 and 0.04 kg/s respectively, and the pressure drop feature a straight line in the converged part. Reynolds number is proportional depending on the flow velocity and the inversely on the dynamic viscosity of fluid, as flow rate increases the Re number increases and vice versa. The table below, represents the effect of flow rate on pressure drop and friction factor.

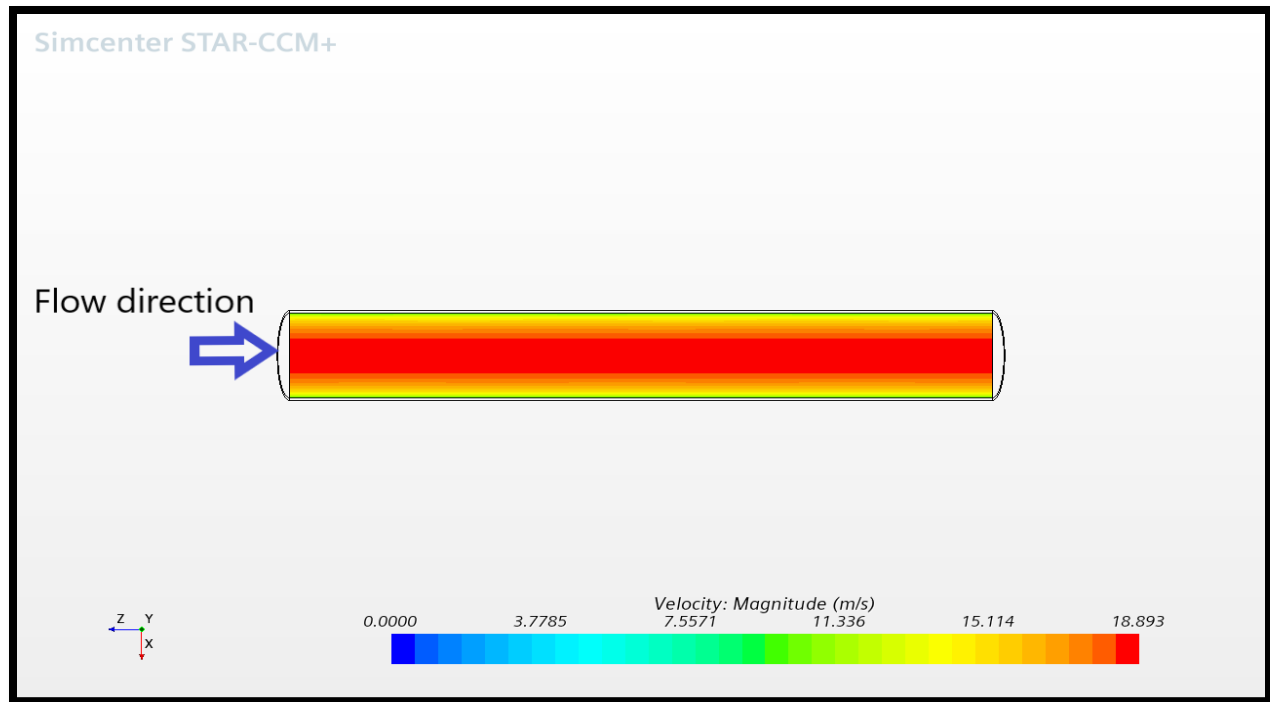
\dot{m} (kg/s)	L (m)	r_i (m)	u (m/s)	ρ (kg/m ³)	μ (Pa. s)	Δp (Pa)	f	Re
0.025	0.5	0.033	13.24	1.11	2.03E-05	14.13	0.01	2.38E+04
0.03	0.5	0.033	15.89	1.11	2.03E-05	20.16	0.01	2.86E+04
0.04	0.5	0.033	21.19	1.11	2.03E-05	34.67	0.01	3.82E+04

Table 11 Pressure drops, and friction factor results for smooth tube

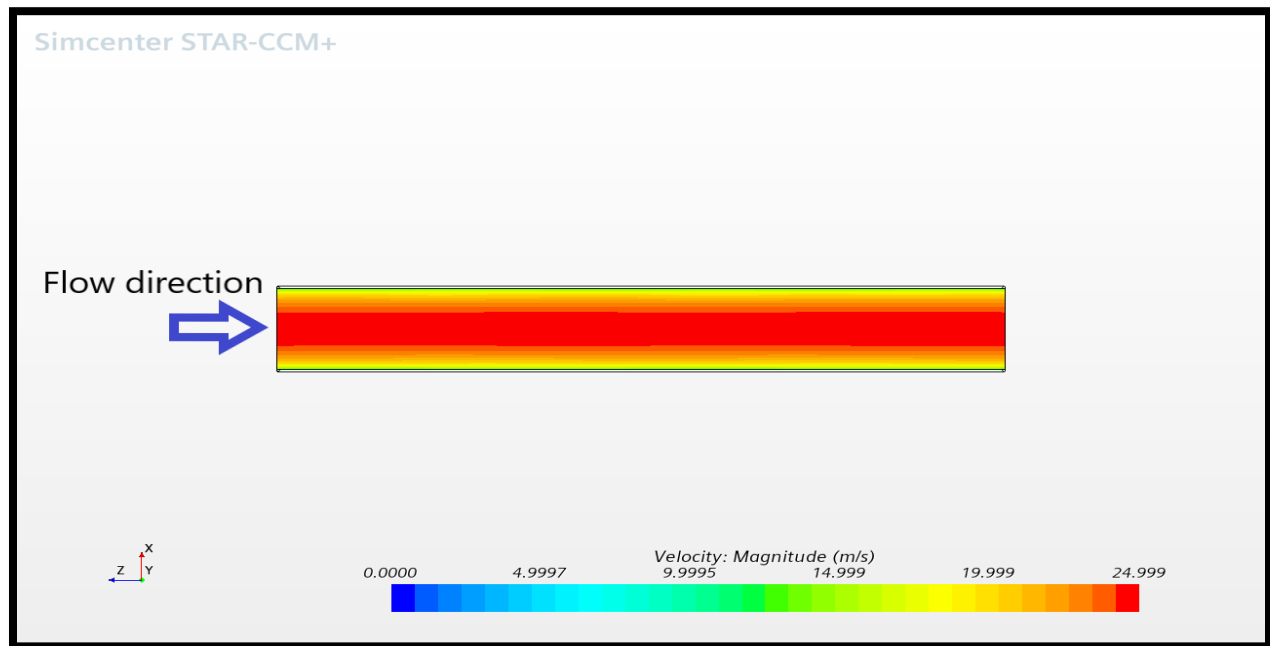
As the velocity of fluid increases the pressure drop will be increased, similarly the greater friction, more resistance to motion is going to happen. It seems that the parameters of flow are constant function of temperature but there is no heat applied therefore, the parameters close to the inlet value of temperature.



(a)



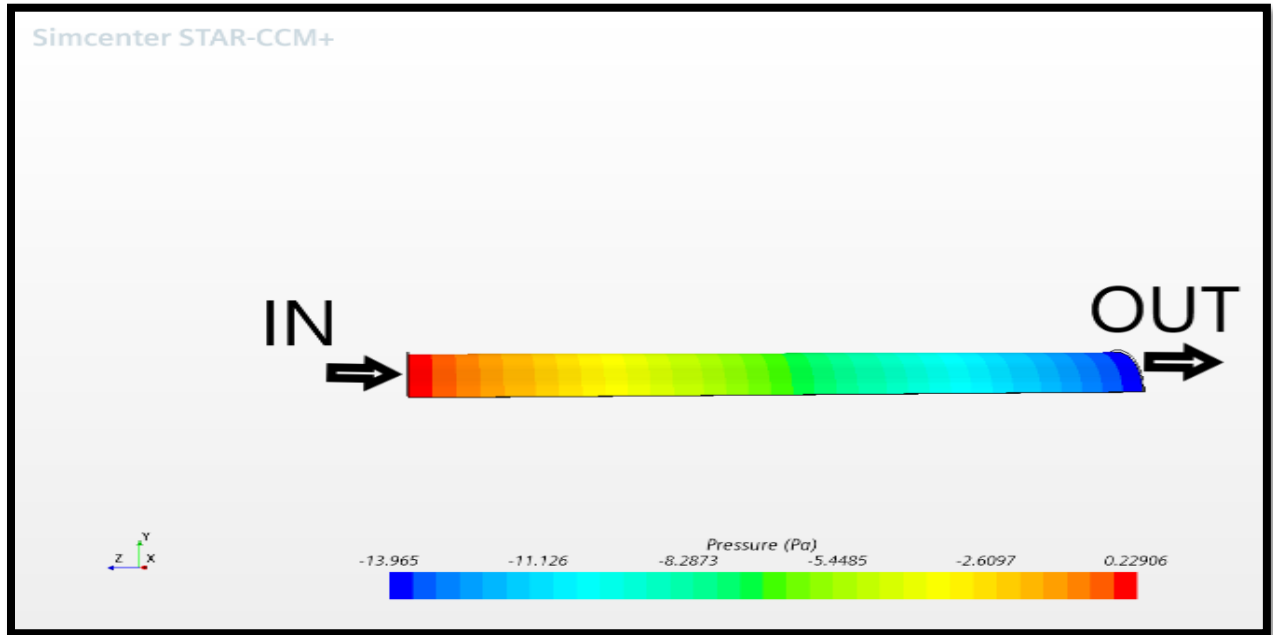
(b)



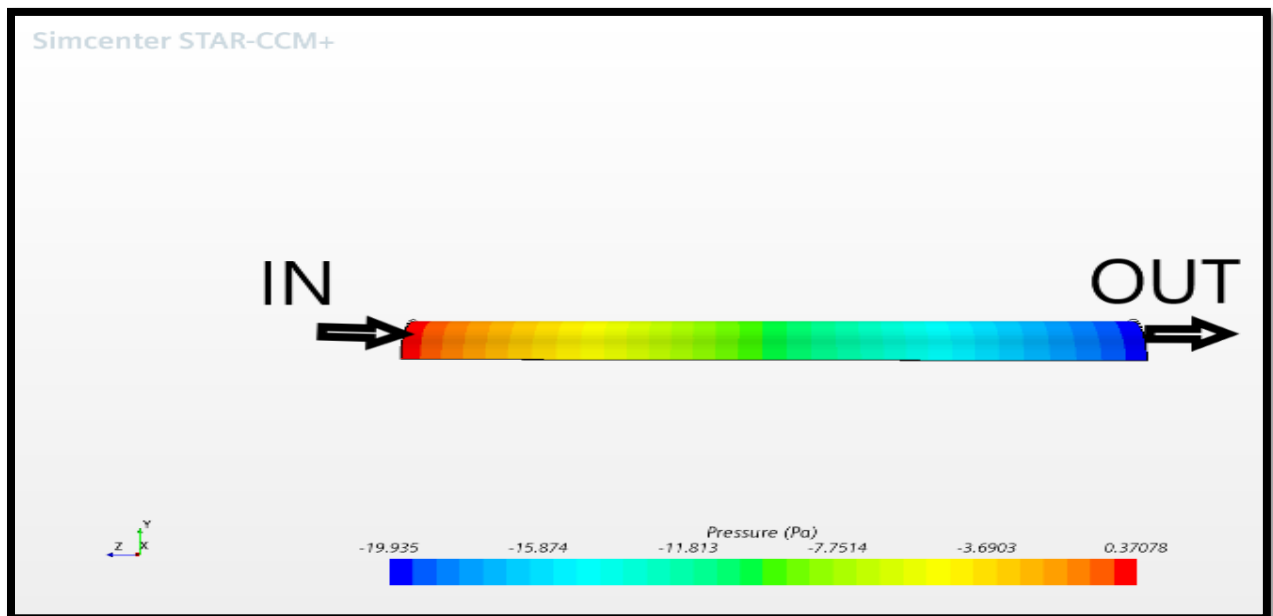
(c)

Figure 12.1 Velocity profile of smooth tube for different mass flow rates (a) 0.025 (b) 0.03
(c) 0.04 kg/s

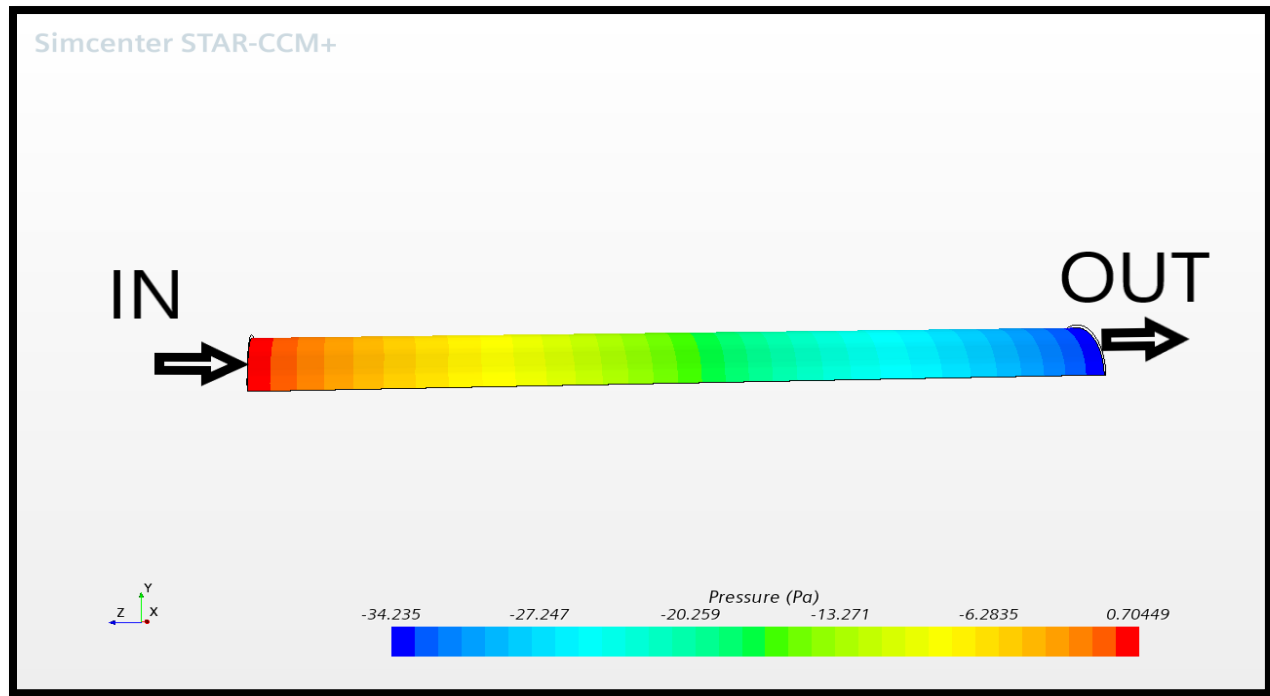
The derived parts in Star ccm+ is applied to represent figures and streamlines of a system, these cross sections obtained at the bottom side of half-tube in a symmetry plane considering only fluid internal tube. as mass flow increases the velocity of fluid increases.



(a)



(b)



(c)

Figure 4.2 Pressure distribution inside the smooth tube for different mass flow rates (a) 0.025 (b) 0.03 (c) 0.04 kg/s

In these figures, pressure at the inlet has higher value in compared with outlet this due to friction and resistant of fluid inside the tube with wall, the pressure drop is reached by subtracting the outlet pressure from inlet pressure.

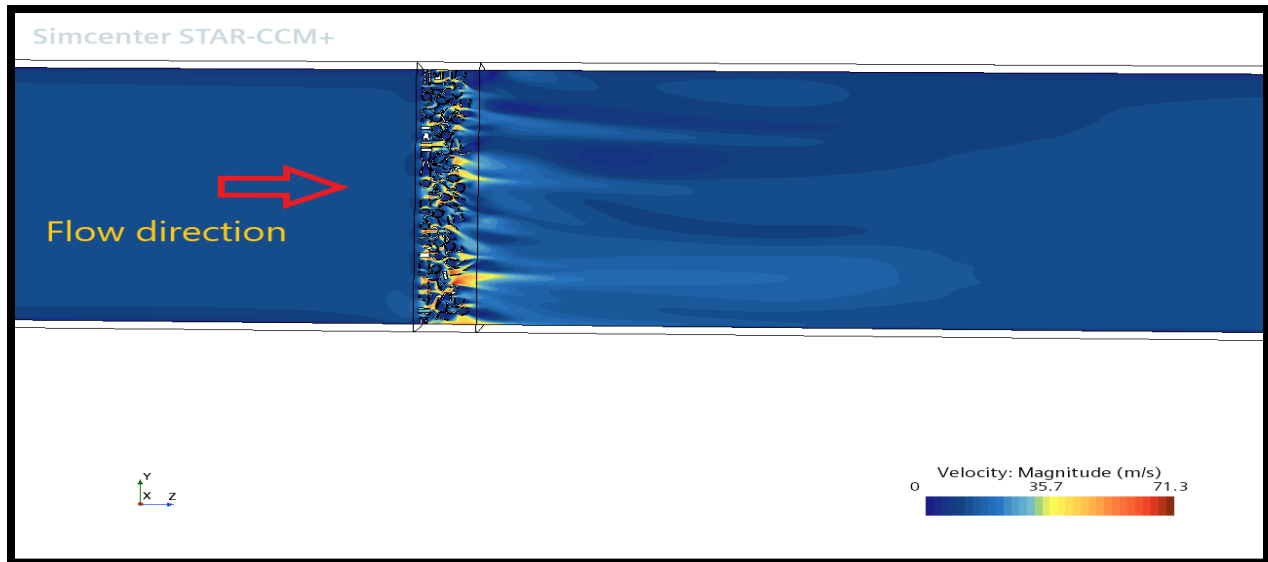
4.1.2 Raschig rings

Raschig rings inserted in the center of tube and applying the same boundary conditions and simulation set up of smooth tube, the pressure drops researched highest amount due to rings that make obstacles to let the fluid moves smoothly inside the tube.

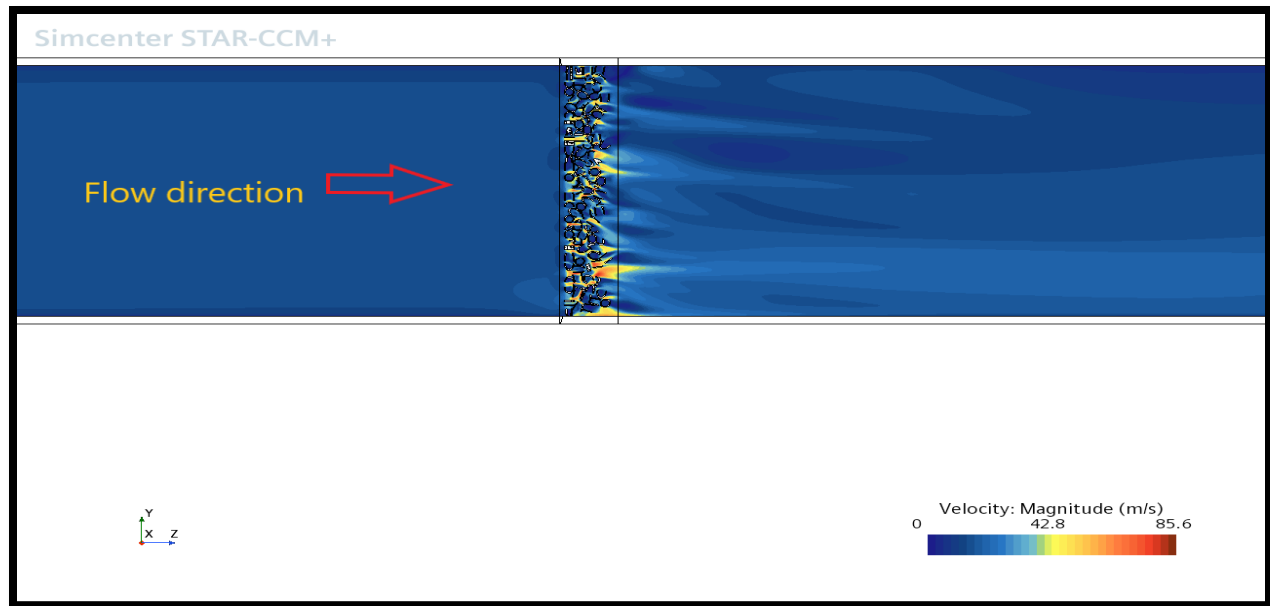
\dot{m} (kg/s)	L (m)	r_i (m)	u (m/s)	ρ (kg/m ³)	μ (Pa.s)	Δp (Pa)	f	Re
0.025	0.5	0.033	12.14	1.204	2.02E-05	4204.69	3.13	2.39E+04
0.03	0.5	0.033	14.59	1.204	2.02E-05	5960.62	3.07	2.87E+04
0.04	0.5	0.033	19.45	1.204	2.02E-05	10398.89	3.01	3.83E+04

Table 12 Pressure drops, and friction factor results for tube with RRs

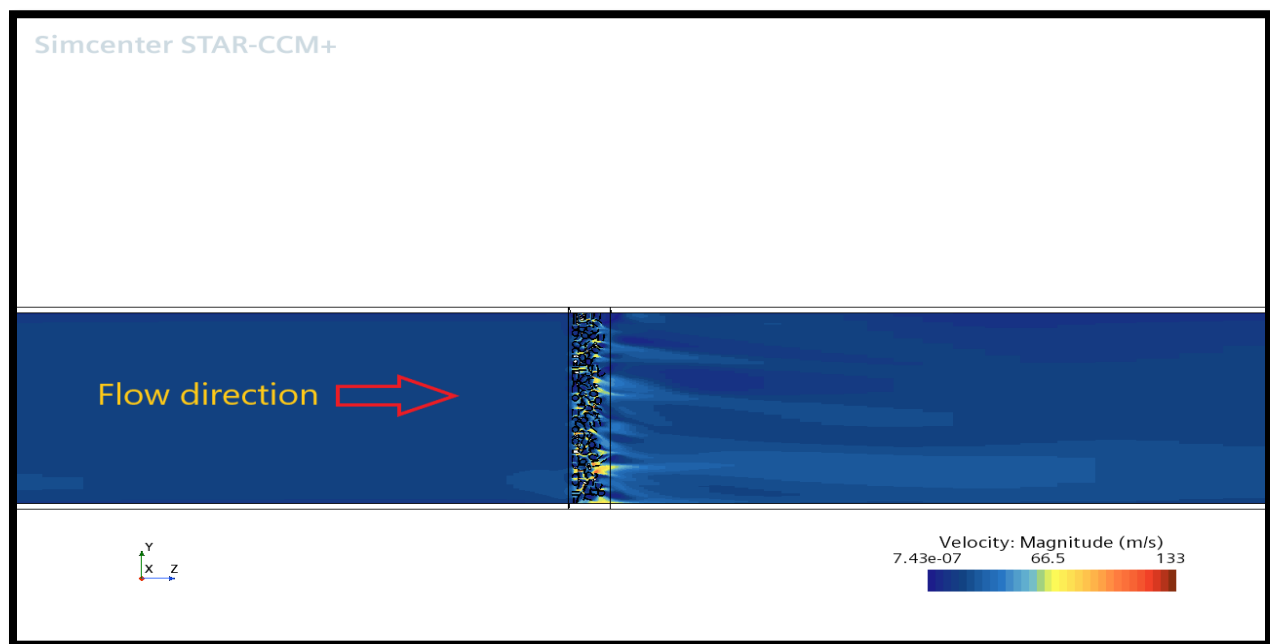
These pressures drop depend on the porosity of the porous medium a small change in the porosity has a large impact on the pressure drop and thus this effect can have a large influence on the pressure drop, predicted by the models. There are different models to predict the pressure drop inside the bed.



(a)



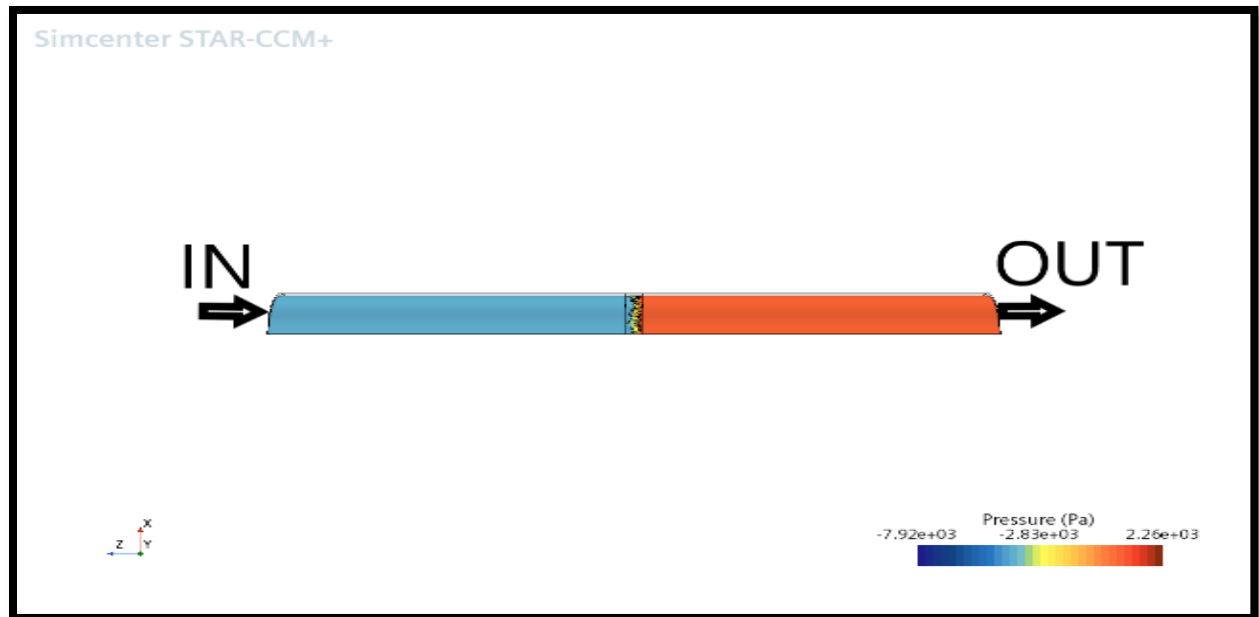
(b)



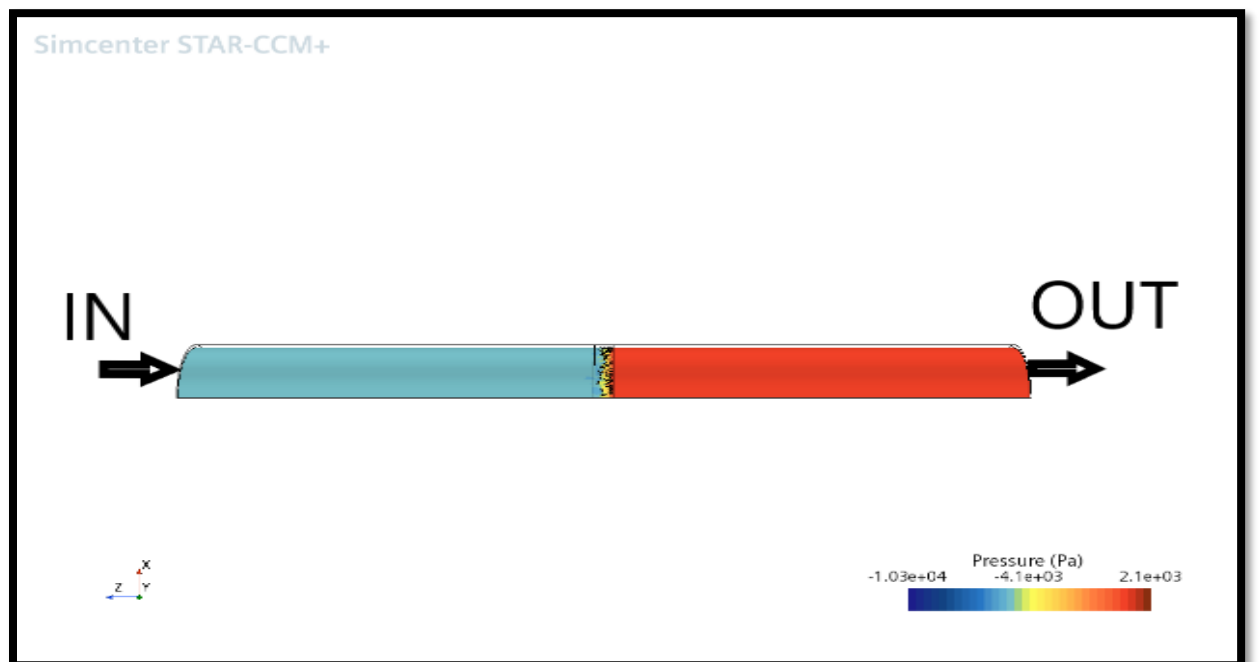
(c)

Figure 13 Velocity profile of smooth tube for different mass flow rates (a) 0.025 (b) 0.03
(c) 0.04 kg/s

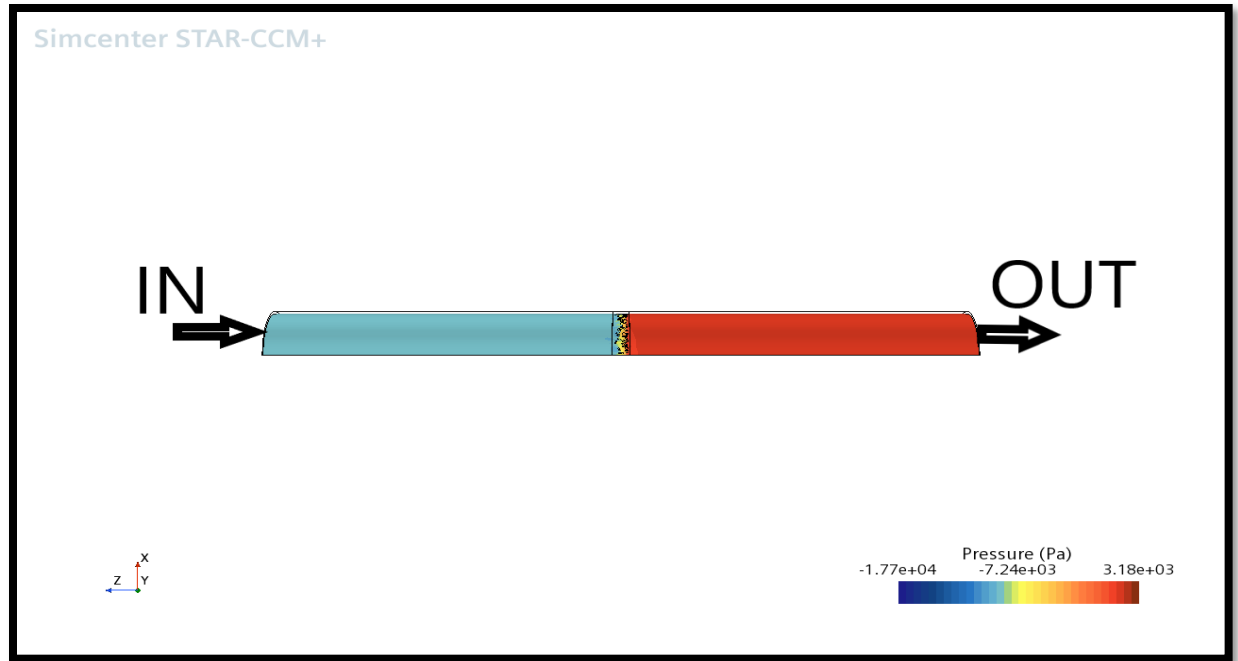
The velocity of fluid increased inside the rings comparing with the rest of the parts of tube the reason beyond that the area of flow has been decreased by these rings that cannot allow the fluid moves in the same area.



(a)



(b)



(c)

Figure 4.4 Pressure distribution inside the smooth tube for different mass flow rates (a) 0.025 (b) 0.03 (c) 0.04 kg/s

It is very clear that the effect of Raschig rings inside the tube, in the side before the Raschig rings there is not any effect of pressure, the outlet side after the Raschig rings, the pressure reached the maximum value due to many reasons mentioned previously.

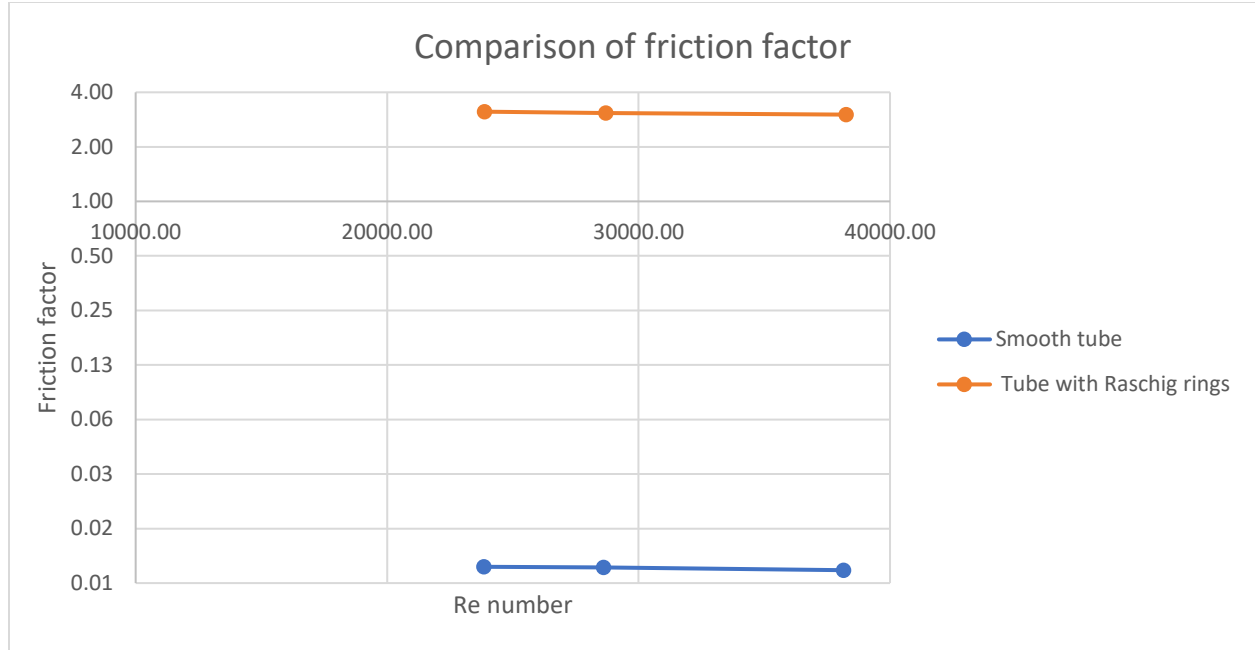


Figure 14 Friction factor comparison between smooth tube and enhanced pipes derived from numerical results

There is a very common difference between smooth tube and enhanced tube in term of friction factor which mainly depend on pressure drop.

4.2 Thermal effects

To assess the thermal performance of the model, average Nu numbers are calculated from convective heat transfer coefficient, applying useful heat for three different mass flow rates 0.025, 0.03 and 0.04 kg/s.

For periodic boundary conditions, as mentioned before fully developed interface for inlet and outlet are applied. Moreover, the surface average of wall interface between the fluid and the solid part is considered.

$$Q_{useful} = \dot{m} * c_p * (T_{out} - T_{in}) \quad (15)$$

$$h_m = \frac{Q_{useful}}{A*(T_w - T_m)} \quad (16)$$

$$T_m = \frac{T_{in} + T_{out}}{2} \quad (17)$$

Table 14

$$Nu_m = \frac{h_m * D_{ri}}{k} \quad (18)$$

$$Nu = 0.023 * Re^{0.8} * Pr^{0.4} \quad (19)$$

$$Re = \frac{4 * \dot{m}}{\pi * D_{ri} * \mu} \quad (20)$$

$$Pr = \frac{\mu * cp}{k} \quad (21)$$

4.2.1 Smooth tube

To begin this comparison, validations were carried out for a full smooth tube with Dittus-Boelter correlation, thus the length of tube used in the study was 1 m to have an agreement of $\frac{L}{D} > 10$, the mass flow is double of those considered for a half tube and the percentage of error is around 10-20%.

D_i (m)	\dot{m} (kg/s)	A_f (m ²)	μ (Pa. s)	ρ (Kg/m ³)	u (m/s)	Re	cp (J/kg K)	Pr	Nu correlation
0.066	0.05	3.42E-03	2.52E-05	0.972	19.92	50689.29	1025.44	0.70	116.01
0.066	0.06	3.42E-03	2.44E-05	0.98	19.59	52062.12	1021.69	0.71	118.66
0.066	0.08	3.42E-03	2.44E-05	1.016	26.76	73445.73	1020.85	0.70	156.23

Table 13.3 Average Nusselt correlation results

Nu number correlation mainly depends on the Re number, as it seems that the Pr number has no real effect on the results therefore, as Re number increases the Nu increases and vice versa.

T_{in} (K)	T_{out} (K)	T_m (K)	T_w (K)	q (W/m ²)	K (W/m k)	Q (W)	A_s (m ²)	h_m (W/m ² K)	Nu_m
300.00	523.72	411.86	1404.13	50000	0.037	11470.53	0.21	55.78	100.12
300.00	459.92	379.96	1271.84	50000	0.035	9803.32	0.21	53.04	99.23
300.00	451.74	375.87	1170.10	50000	0.035	12391.92	0.21	75.29	140.50

Table 15.4 Average Nusselt obtained from Star ccm+

The average Nu number related proportionally to convective heat transfer coefficient, this simulation runs till 10000 iterations to get convergent but still they did not get it due to time it is considered that the second value should be higher than the first value in term of convective heat transfer and average Nu number.

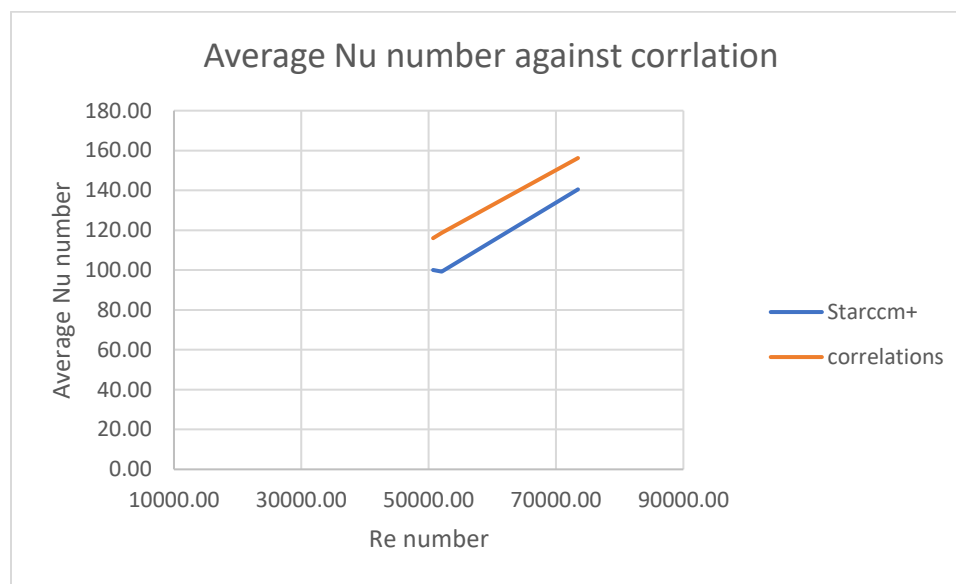


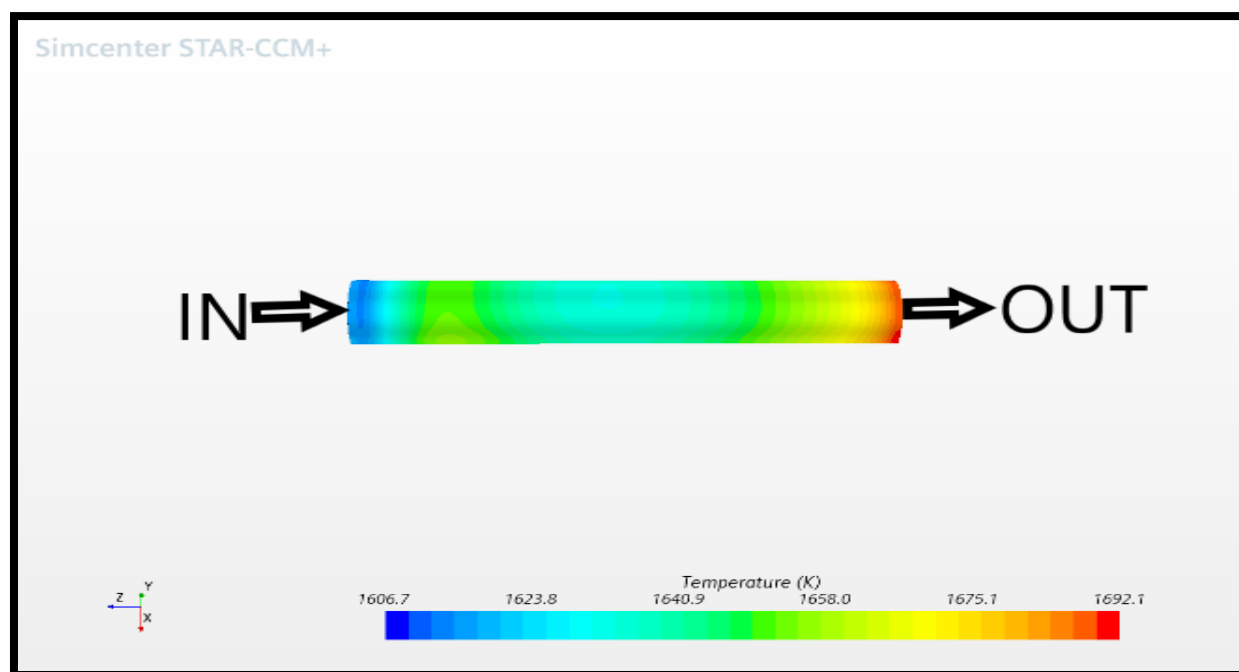
Figure 4.6 Average Nu number for full tube

The average Nu number of correlations should have less value than value obtained from the star ccm+ but as mentioned before the iterations still need time to get converged and the error is calculated between 10-15%. After all these procedures half tube is going to be considered for the next process,

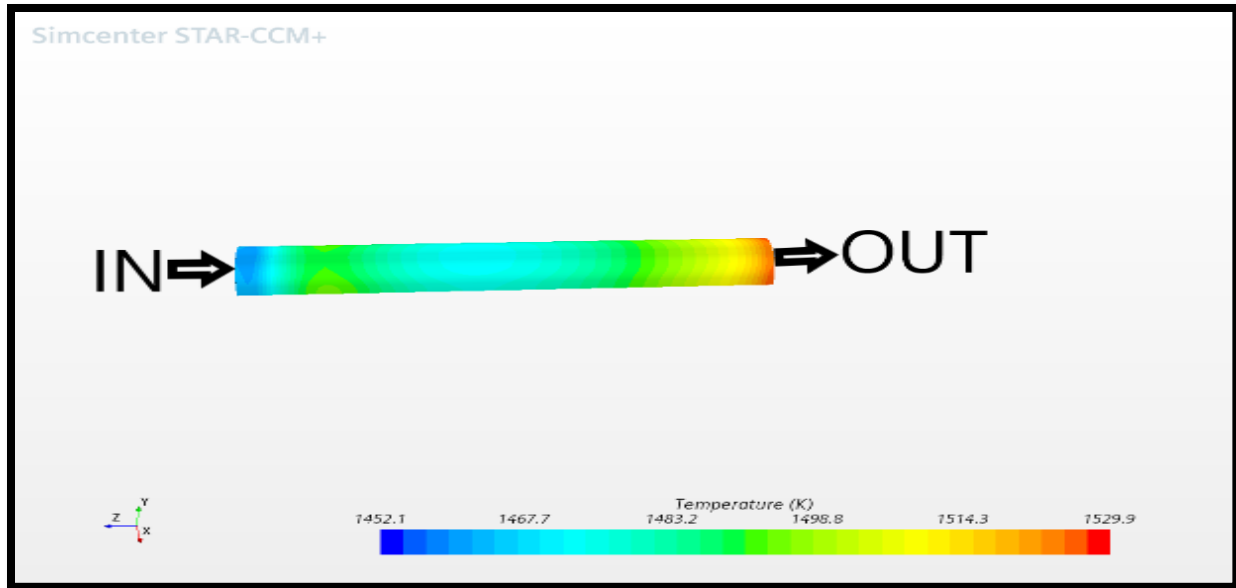
T_{in} (K)	T_{out} (K)	T_m (K)	T_w (K)	q (W/m ²)	K (W/m k)	Q (W)	A_s (m ²)	h_m (W/m ² K)	Nu_m
300	408.51	354.25	1639.56	50000	0.037	2785.76	0.05	41.83	37.50
300	389.82	344.91	1480.44	50000	0.036	2760.50	0.05	46.92	43.09
300	368.98	334.49	1228.93	50000	0.034	2812.74	0.05	60.70	58.82

Table 16 Average Nu number for smooth tube

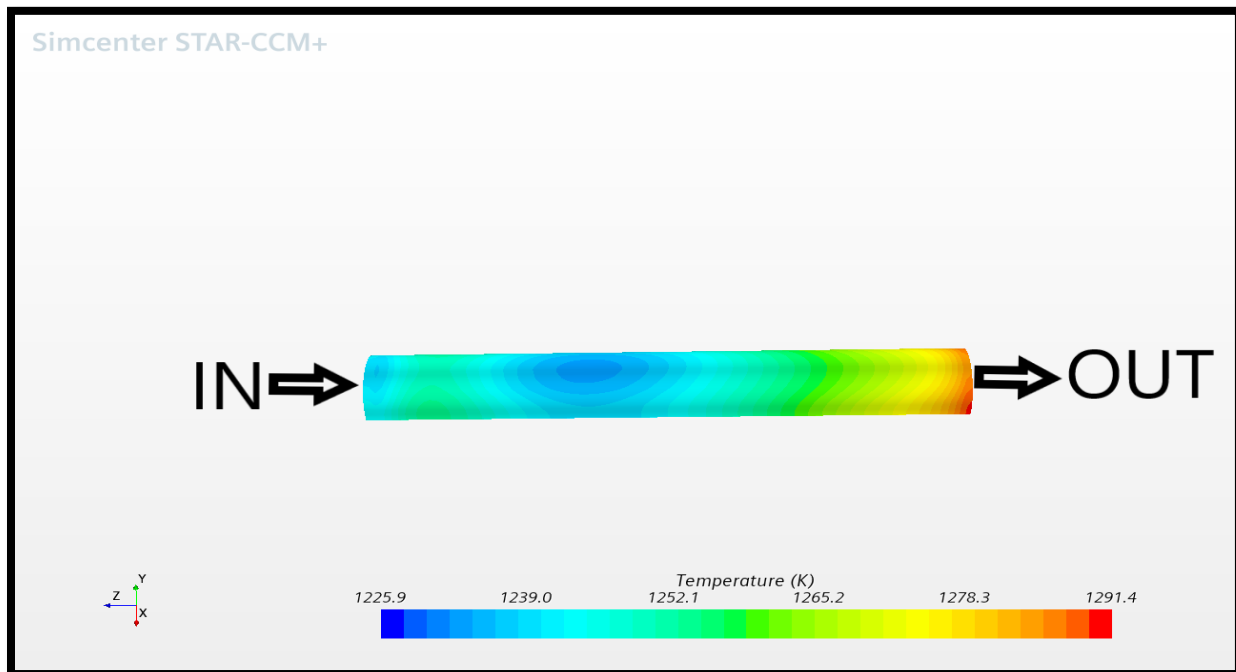
The outlet temperature decreases, when the mass flow increases and the convective heat transfer increases as outlet temperature decreases. The amount of absorbed heat increased as the difference between temperature of wall and mean temperature.



(a)



(b)



(c)

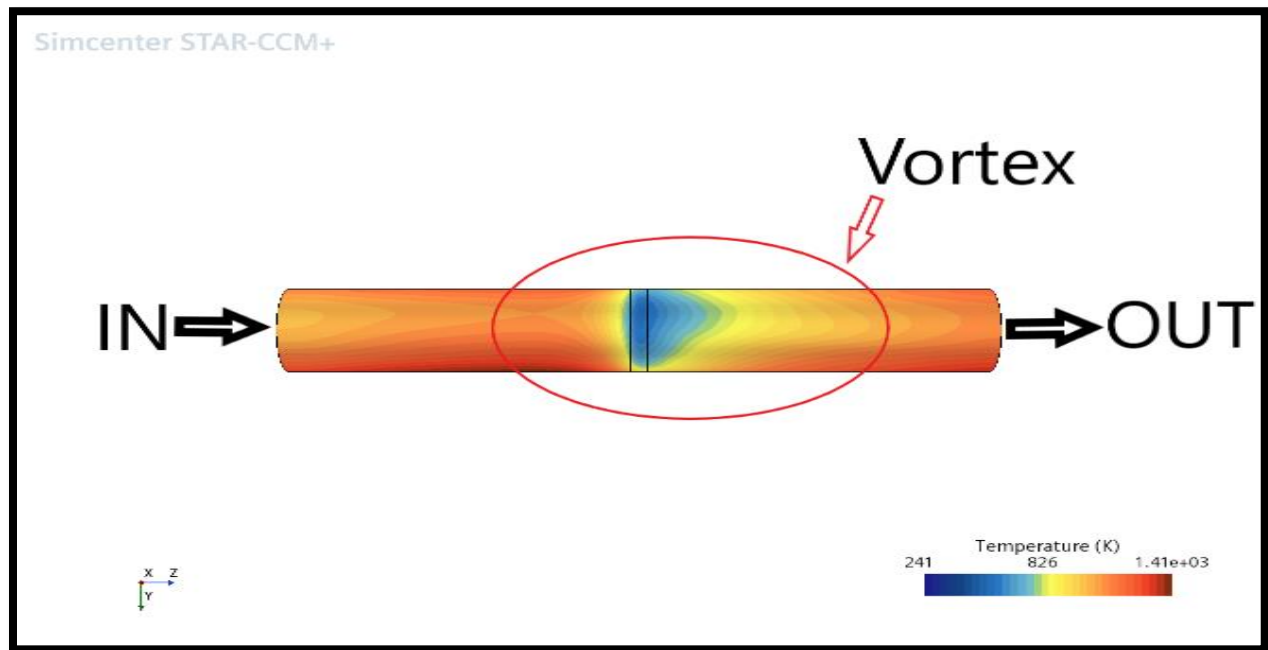
Figure 4.7 Temperature of wall for the smooth tube for different mass flow rates (a) 0.025 (b) 0.03 (c) 0.04 kg/s

As these figures above shows how the temperature of wall are distributed in the surfaces if tube.

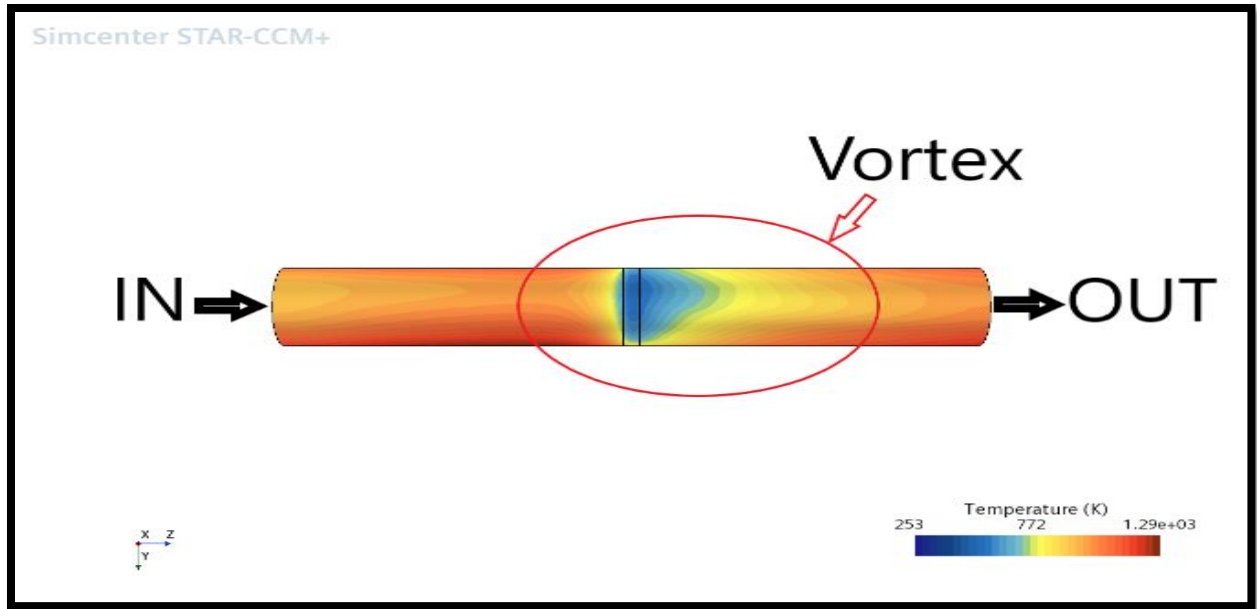
4.2.2 Raschig rings

T_{in} (K)	T_{out} (K)	T_m (K)	T_w (K)	q (W/m ²)	K (W/m k)	Q (W)	A_s (m ²)	h_m (W/m ² K)	Nu_m
300	412.77	356.39	1068.00	50000	0.034	2868.05	0.05	77.79	76.63
300	396.54	348.27	972.64	50000	0.032	2940.51	0.05	90.90	93.74
300	377.94	338.97	848.67	50000	0.031	3159.91	0.05	119.66	127.38

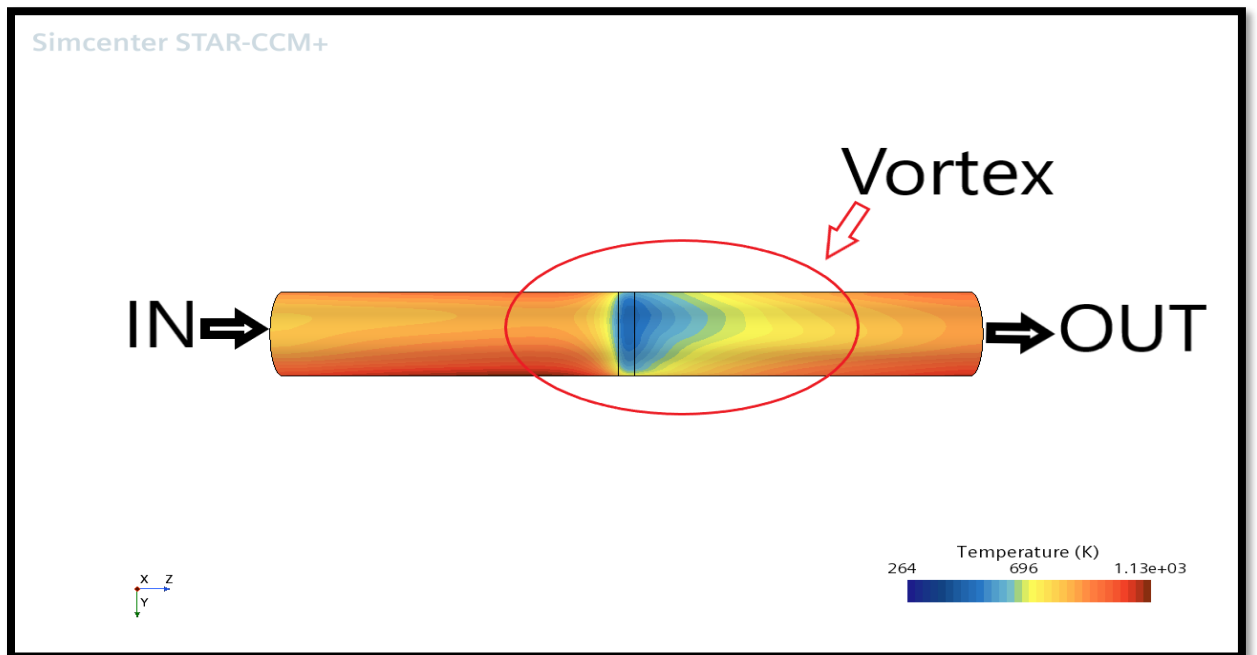
Table 4.6 Average Nusselt results for tube with RRs



(a)



(b)



(c)

Figure 15 Temperature of wall for the tube with RRs for different mass flow rates (a) 0.025 (b) 0.03 (c) 0.04 kg/s

The vortexes are appeared after the Raschig rings due to flux distribution and heat absorbed by rings inside the tube.

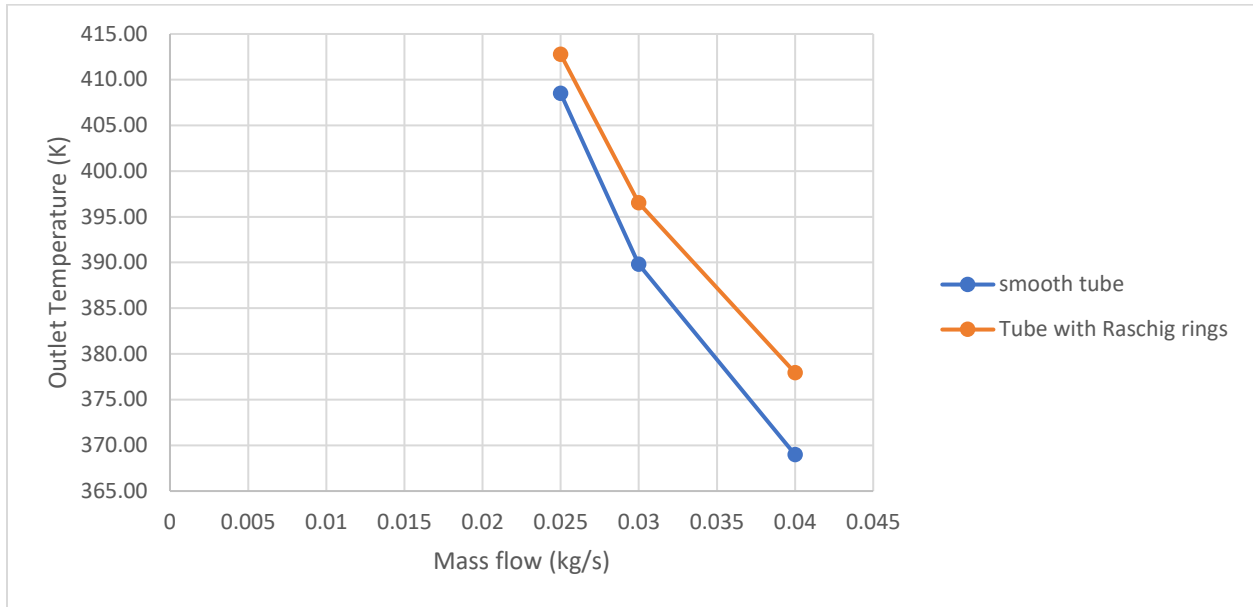


Figure 4.9 Outlet temperatures comparison

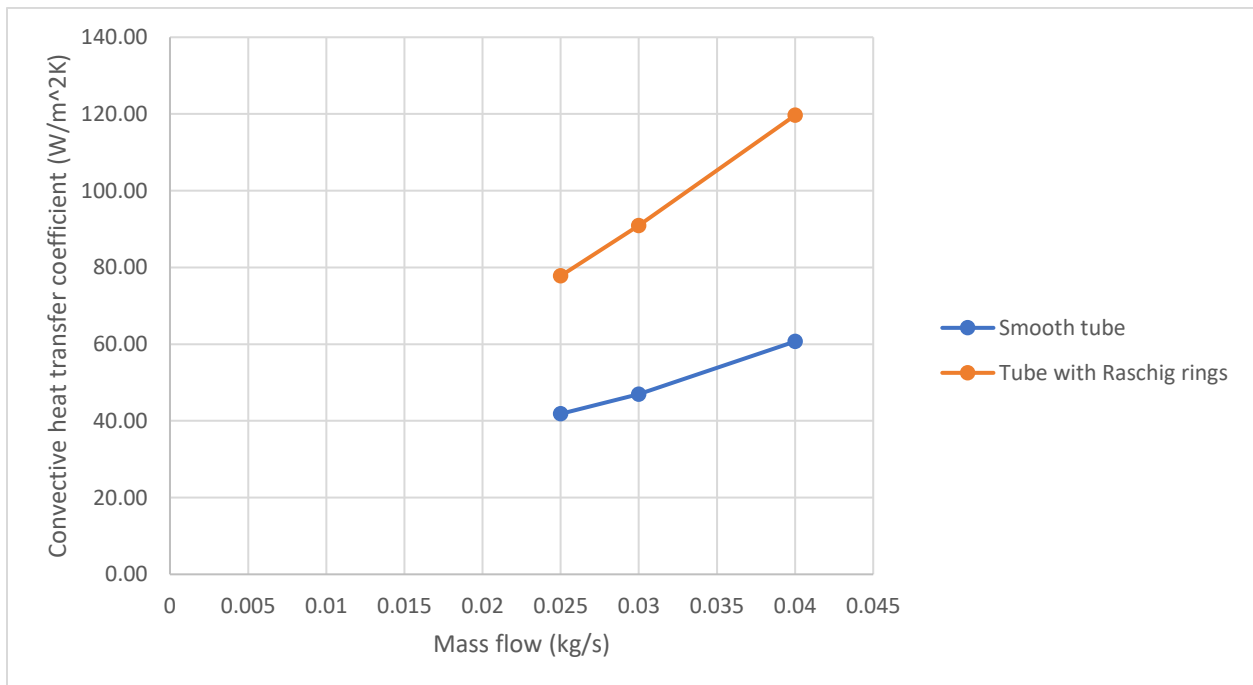


Figure 4.10 Convective heat transfer coefficient comparisons

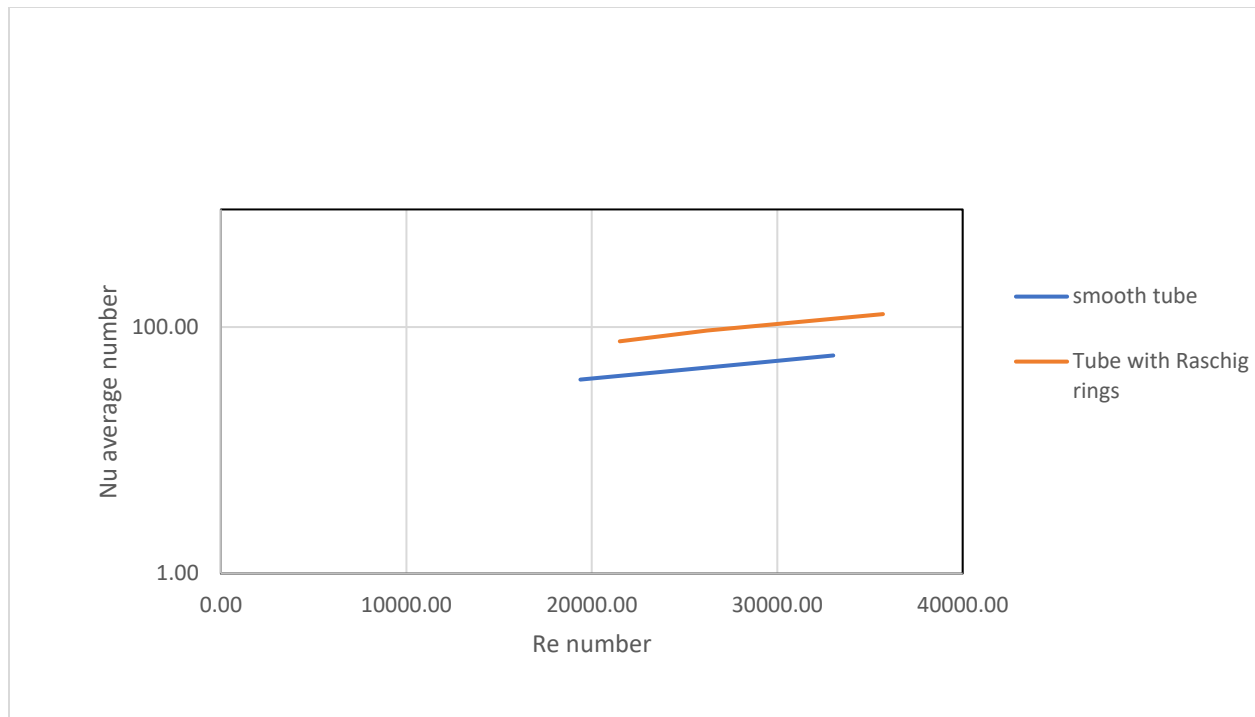


Figure 4.11 Average Nu number comparisons

Chapter five

Conclusion

The goal of this study is to make some improvements into the current Linear Fresnel collector technology. As matter of fact the absorber tube has a significant role in LFC, therefore, a comparison between smooth tube and the proposed tube equipped with Raschig rings are performed to determine how the thermal efficiency of LFC can be improved by equipping the tube with porous medium.

The CFD commercial software STAR-CCM+ is utilized to perform simulations. As the first step, a CFD mesh optimization procedure has been carried out to obtain unique results, in this step two types of fluid have been used to make sure that the optimized mesh works under different types of fluid. Moreover, the fully developed interface boundary conditions for inlet and outlet are set for in all simulations. Following this step validation process showed an agreement between numerical data and literature to guarantee that the results for smooth pipe and pipe with Raschig rings are correct.

The major thermal and hydraulic parameters were computed using three different mass flow rates in the assessment. From the study of hydraulic characteristics, it is obtained that the enhanced pipe produces higher pressure drops due to the porosity and shape of Raschig rings medium compared to the smooth tube and consequently the friction factor increases based on the pressure drop.

Since the focus was only on the effects of Raschig rings, it is assumed to apply a uniform heat flux and neglecting all the losses happen for tube such as radiation and convection losses. The average Nusselt numbers are calculated for a full smooth tube to validate with Dittus-Boelter correlation the results show that a percentage of error around 10-15% which is an acceptable according to the limits defined by literature.

Moreover, the outlet fluid temperatures of pipe with Raschig rings are higher than the smooth tube by 2 to 10 K. These increases temperatures are related to convective heat transfer coefficient and Nu number, as it can clearly mentioned that the convective heat transfer coefficient of tube with Raschig increases around 85% and Nusselt number to the double.

After all, it can be concluded that the tube with Raschig rings has better performance from thermal point of view, however, the pressure drops increases which is not a big concern in this research.

Concerning about further development, solar flux with defined field function must be used, applied as b.c considering convective and radiative losses, another point inserting Raschig rings in different position inside the tube to take the advantage of thermal mixing and may be putting the pours disc closer to inlet.

REFERENCES

- [1] S. A. Kalogirou, *Solar thermal collectors and applications*, vol. 30. 2004.
- [2] B. D. Abbott, “Keeping the Energy Debate Clean : How Do We Supply the World ’ s Energy Needs ?,” vol. 98, no. 1, 2010.
- [3] what is the CSP, “<https://www.brunel.net/en/blog/renewable-energy/concentrated-solar-power>.”
- [4] G. Zhu, T. Wendelin, M. J. Wagner, and C. Kutscher, “History, current state, and future of linear Fresnel concentrating solar collectors,” *Sol. Energy*, vol. 103, pp. 639–652, 2014, doi: 10.1016/j.solener.2013.05.021.
- [5] E. Bellos, E. Mathioulakis, E. Papanicolaou, and V. Belessiotis, “Experimental investigation of the daily performance of an integrated linear Fresnel reflector system,” *Sol. Energy*, vol. 167, no. April, pp. 220–230, 2018, doi: 10.1016/j.solener.2018.04.019.
- [6] C. Zahler, I. S. Gmbh, and C. Wittwer, “The Solarmundo line focussing Fresnel collector . Optical and thermal performance and cost calculations The Solarmundo line focussing Fresnel collector . Optical and thermal performance and cost calculations .,” no. January, 2002.
- [7] A. Hofer, F. Cuevas, A. Heimsath, P. Nitz, W. J. Platzer, and S. Scholl, “Extended Heat Loss and Temperature Analysis of Three Linear Fresnel Receiver Designs,” *Energy Procedia*, vol. 69, pp. 424–433, 2015, doi: 10.1016/j.egypro.2015.03.049.
- [8] M. Günther, “Linear Fresnel Technology,” *Adv. CSP Teach. Mater.*, pp. 1–43, 2011.
- [9] A. Famiglietti and A. Lecuona, “Direct solar air heating inside small-scale linear Fresnel collector assisted by a turbocharger : Experimental characterization,” *Appl. Therm. Eng.*, vol. 196, no. January, p. 117323, 2021, doi: 10.1016/j.applthermaleng.2021.117323.
- [10] L. Savoldi, A. Allio, A. Bonvento, M. Cantone, and J. Fernandez, “Experimental and numerical investigation of a porous receiver equipped with Raschig Rings for CSP applications,” *Sol. Energy*, vol. 212, no. November, pp. 309–325, 2020, doi: 10.1016/j.solener.2020.11.006.
- [11] E. Bellos and C. Tzivanidis, “Multi-criteria evaluation of a nanofluid-based linear Fresnel solar collector,” *Sol. Energy*, vol. 163, no. October 2017, pp.

- 200–214, 2018, doi: 10.1016/j.solener.2018.02.007.
- [12] E. Bellos, “Enhancing the performance of a linear Fresnel reflector using nanofluids and internal finned absorber,” *J. Therm. Anal. Calorim.*, vol. 135, no. 1, pp. 237–255, 2019, doi: 10.1007/s10973-018-6989-1.
 - [13] K. R. Kumar and K. S. Reddy, “Thermal analysis of solar parabolic trough with porous disc receiver,” *Appl. Energy*, vol. 86, no. 9, pp. 1804–1812, 2009, doi: 10.1016/j.apenergy.2008.11.007.
 - [14] C. Yang, Y. Zhang, F. Yan, W. Zhang, and W. Li, “The numerical simulation of enhanced heat transfer on a Linear Fresnel molten salt-type receiver tube filled with porous media,” vol. 01041, pp. 4–9, 2019.
 - [15] S. Steel, “<https://www.montanstahl.com/blog/stainless-steel-sections-solar-power-plants/#:~:text=The%20natural%20properties%20of%20stainless%20steel%20make%20them,where%20these%20solar%20power%20plants%20are%20often%20based.>”
 - [16] S. Bottillo, A. D. L. Vollaro, G. Galli, and A. Vallati, “ScienceDirect Fluid dynamic and heat transfer parameters in an urban canyon,” *Sol. Energy*, vol. 99, pp. 1–10, 2014, doi: 10.1016/j.solener.2013.10.031.
 - [17] P. D. I. Milano, “Politecnico di milano,” no. i, 2019.
 - [18] R. Zanino, R. Bonifetto, J. M. Christian, C. K. Ho, and L. S. Richard, “Effects of RANS-Type turbulence models on the convective heat loss computed by CFD in the solar two power tower,” vol. 49, pp. 569–578, 2014, doi: 10.1016/j.egypro.2014.03.061.
 - [19] T. S. Phillips and C. J. Roy, “Richardson Extrapolation-based Discretization Uncertainty Estimation for Computational Fluid Dynamics,” vol. 1, no. 1, pp. 1–17, 2014.
 - [20] A. Standard for Verification and Validation in Computational Fluid Dynamic and Heat Transfer, “GCI-5steps_procedure.” pp. V&V 20, 2009.
 - [21] www.simscale.com/docs/simwiki/numerics-background/what-are-boundary-conditions/, “Boundary conditions.”
 - [22] W. Zhong, K. Xu, X. Li, Y. Liao, G. Tao, and T. Kagawa, “Determination of pressure drop for air flow through sintered metal porous media using a modified Ergun equation,” vol. 27, pp. 1134–1140, 2016, doi: 10.1016/j.appt.2016.03.024.

- [23] D. Nemec and J. Levec, “Flow through packed bed reactors: 1. Single-phase flow,” *Chem. Eng. Sci.*, vol. 60, no. 24, pp. 6947–6957, Dec. 2005, doi: 10.1016/j.ces.2005.05.068.
- [24] J. M. Villora, P. Callejas, M. F. Barba, and C. Baudí, “Statistical analysis of the fracture behaviour of porous ceramic Raschig rings,” vol. 24, pp. 589–594, 2004, doi: 10.1016/S0955-2219(03)00245-0.
- [25] A. G. Dixon, M. Nijemeisland, and E. H. Stitt, “Systematic mesh development for 3D CFD simulation of fixed beds : Contact points study,” vol. 48, pp. 135–153, 2013.
- [26] T. Eppinger, K. Seidler, and M. Kraume, “DEM-CFD simulations of fixed bed reactors with small tube to particle diameter ratios,” vol. 166, pp. 324–331, 2011, doi: 10.1016/j.ces.2010.10.053.